Article

Characterization of Bentonites from the *in situ* ABM5 Heater Experiment at Äspö Hard Rock Laboratory, Sweden

Ana María Fernández[1,*], José F. Marco[2], Paula Nieto[1], Fco. Javier León[1], Luz María Robredo[1], M. Angeles Clavero[1], Ana Cardona[1], Sergio Fernández[1], Daniel Svensson[3] and Patrik Sellin[3]

[1] CIEMAT, Departamento de Medio Ambiente, Madrid, Spain; anamaria.fernandez@ciemat.es
[2] CSIC, Instituto de Química Física "Rocasolano", Madrid, Spain; jfmarco@iqfr.csic.es
[3] Department of Research and Safety Assessment, SKB—Svensk Kärnbränslehantering, Stockholm, Sweden; daniel.Svensson@skb.se (D.S.); patrik.sellin@skb.se (P.S.)
* Correspondence: anamaria.fernandez@ciemat.es

Abstract: The Alternative Buffer Material ABM5 experiment is an *in situ* medium-scale experiment performed at Äspö Hard Rock Laboratory (HRL) conducted by SKB in Sweden with the aim of analysing the long-term stability of bentonites used as engineering barrier for a high-level radioactive waste repository (HLWR). In this work, four different ring-shaped Ca- and Na-bentonite blocks, which were pilled around a carbon steel cylindrical heater, subjected to a maximum temperature of 250°C and hydrated with saline Äspö groundwater (0.91 M ionic strength), were characterized after dismantling by using different techniques (XRD, FTIR, XRF, Mössbauer, squeezing, etc.). This work allowed to identify the main geochemical processes involved in this system, as well as the modifications in physico-chemical properties and pore water chemistry after 4.4 years of treatment. No significant modifications in mineralogy were observed in samples close to heater contact, except an increase in Fe content due to C-steel corrosion, carbonate dissolution/precipitation (mainly calcite and siderite) and Mg increase. No magnetite and low amount of Fe(II) inside the clay mineral structure were detected, indicating prevalence of oxidizing conditions. No modifications were observed in smectite structure, except a slight increase in total and tetrahedral charge. A decrease in external surface area and CEC was detected in all samples, lower values being more stressed at the heater contact. It seems that temperature and water vapor fluxes have affected to CEC parameter, due to the differences observed from top to bottom of the bentonite column. As consequence of the advective-diffusion infiltration of the saline Na-Ca-Cl Äspö groundwater, a modification of the composition at clay mineral exchange sites occurred with a tendency to achieve equilibrium in all types of bentonites. Ca-bentonites increased their Na content at exchange sites whereas Na-bentonite increased their Ca content. Exchangeable Mg content decreased in all bentonites, except in MX-80 located at the bottom part of the package. The initial bentonite pore water was modified after their interaction with the saline groundwater. A salinity gradient is observed through the bentonite blocks from the granite to heater contact, lower ionic strengths being detected at the bottom part of the bentonite column probably due to the higher degree of saturation in this zone. Thus, no geochemical equilibrium conditions were achieved after 4.4 years of experiment.

Keywords: Bentonites; Smectites; Pore water chemistry; Mineralogy, Cation exchange, ABM-Experiment; large-scale tests.

Citation: Lastname, F.; Lastname, F.; Lastname, F. Title. *Minerals* **2021**, *11*, x. https://doi.org/10.3390/xxxxx

Academic Editor: Firstname Lastname

Received: date
Accepted: date
Published: date

1. Introduction

Bentonites are an essential component of the multi-barrier system securing the long-term safety of the final disposal of nuclear wastes. The efficiency of such engineering clay barrier system (EBS) relies on its physical and chemical confinement properties: low permeability, low diffusivity, high retention and swelling capacity. Therefore, an important issue for performance assessment purposes is to have confidence and demon-

strate the long-term preservation of these properties over the long term, i.e., hundreds of thousands of years under real conditions of a repository.

The scientific approach used to tackle the problem of predicting long-term clay barrier behaviour is by analysing the results from experiments conducted in underground research laboratories (URL) at real scale, real conditions and for long test times: Äspö in Sweden, Mont Terri and Grimsel in Switzerland, Meuse/Haute-Marne in France. Different *in situ* large-scale EBS experiments have been performed over time since 1989 by using both compacted bentonite (e.g., FEBEX *in situ* test, LOT, Prototype, TBT) and high-density bentonite pellets (e.g., RESEAL test, EB experiment, FE experiment).

The Alternative Buffer Material (ABM) experiment is a field medium-scale experiment performed at Äspö Hard Rock Laboratory (HRL) in Sweden with the aim of analysing the long-term stability of different bentonites under similar conditions of the current Swedish concept for high-level radioactive waste repository (HLWR), and under adverse conditions regarding to temperature. The test, conducted by SKB (Swedish Nuclear Fuel and Waste Management Company) is based on the KBS-3 (kärnbränslesäkerhet, nuclear fuel safety) concept, in which a repository will be placed at approximately 500 m depth in crystalline rock, and a buffer of compacted clay will surround corrosion resistant copper canisters containing the waste, in order to minimize water flow and radionuclide transport to the granite host rock.

The ABM experiment includes medium-scale test packages, each one consisting of a central carbon steel tube with heaters, and a buffer of compacted clay being artificially hydrated. Eleven different clays were chosen for the buffers to examine effects of smectite content, interlayer cations and overall iron content. Besides, bentonite pellets with and without additional quartz are being tested. The buffer in package 1 (2006-2009) and package 2 (2006-2013) had been subjected to artificial wetting by formation water and heating for 28 months (at 130°C for ~ 1 year) and 6.5 years (at 141°C after the first 2 years), respectively; and then were retrieved and analyzed. The main purposes of the project were to characterize the clays with respect to hydro-mechanical properties, mineralogy and chemical composition and to identify any differences in behaviour or long-term stability. Besides, the diversity of clays and the heater of steel also make the experiment suitable for studies of iron-bentonite interactions [1].

The ABM45 project started in 2012, including three new packages (4, 5 and 6). ABM5 experiment was running until 2017 when it was retrieved. ABM3 (2006-), ABM4 (2012-) and ABM6 (2012-) are still running and expected to be excavated in 2024. The ABM5 test, represents the worst-case scenarios of an HLWR repository since is one of the hottest bentonite tests (up to 250°C) conducted in an underground research laboratory (URL).

The aim of this work is to analyze the geochemical processes observed in some bentonite samples obtained after dismantling of the ABM5 *in situ* experiment. The dismantling of this test allowed to quantify the modifications of the bentonites after reacting due to changes in the initial physico-chemical conditions and different types of perturbations: a) interactions with artificial granitic groundwater (saturation phase), b) heat (boiling and desaturation phase due to heating), c) perturbations linked to the interactions between the bentonite and the allochthonous engineered solid materials (concrete, C-steels and other metals, iron, organics, etc.), and d) interactions with different gases produced and consumed in the system due to mineral dissolution/precipitation, microbiological reactions and corrosion processes.

2. Materials and Methods

2.1. ABM5 experiment

The project ABM45 (Alternative Buffer Materials 45) is a field experiment consisting of three packages (4, 5, and 6), each one containing 30 ring-shaped bentonite blocks pilled around a cylindrical tube made of carbon steel P235TR1 (Table 1, Figure 1). An electrical heater of 1000 W was placed inside the tube as a heat source. The packages were installed in boreholes (30 cm diameter and 3 m depth) drilled in the TASD tunnel at ca. 420 m depth in the Äspö Hard Rock Laboratory [2]. The granitic host rock consists of Äspö di-

orite and greenstone. The aim of the test was to study and compare the alteration of different bentonite qualities due to groundwater saturation, heating and interaction with corroding metals.

The package 5 was deposited in hole KD0098G01, where there was a groundwater inflow of around 8.5 L/day, coming from a fracture located 0.8 m down from the floor. However, an artificial water saturation system was used for a rapid saturation of the bentonite. The heating test duration was of 4.4 years, starting on November 15th 2012 and finishing on April 10th 2017. The bentonite was heated to 50°C for the first three and half years, to support saturation and prevent water boiling, and then in 2016 the temperature was increased stepwise to 150°C and up to 250°C at heater interface for about the last six months of exposure (Figure 2). Estimated maximum temperatures at heater contact of 240-250°C were reached between blocks 22 and 8, decreasing temperatures both at bottom and top part of the bentonite column (<188-156°C, blocks 3 and 27), and as a function of the granite contact (Figure 2). In the hottest blocks, more than 150°C was reached at a distance of 6 cm from the heater, the thickness of the bentonite block being of 10 cm (see also [3,4]).

The bentonites selected for this experiment were of 12 types: MX-80 2012, Asha 505 2011, Asha NW BFL-L, Deponit CA-N, Febex 2012, Ikosorb 2011, Rokle 2012, Kunigel V1, GMZ 2011, Saponite 2012, Calcigel 2012 and Ibeco SEAL M-90 (old batch). At least two blocks of each bentonite were placed in the test, except for MX-80 and Asha NW BFL-L, for which 5 and 3 blocks were set, respectively. Therefore, 28 bentonite blocks as compacted rings penetrated by the heater were placed inside the hole. Additional MX-80 blocks (#1 and #30) were positioned at top and bottom to secure a tight sealing. After installation of the test package in the test hole, concrete plugs were casted above the test hole in order to prevent the bentonite from swelling up.

The ring-shaped blocks (~27.73 cm outer diameter, ~11.0 cm inner diameter and 10 cm height) were compacted uni-axial in a special mould with a pressure between 50 and 100 MPa. A thin layer of molybdenum sulphide containing grease was applied on all steel surfaces in contact with the bentonite powder in order to lubricate to decrease friction. The grease was removed mechanically from the blocks surfaces prior to bentonite be installed in the test [2].

The outermost slot between bentonite blocks and rock was filled with gravel (2-80 mm), in which 6 mm-diameter titanium tubes with small holes, covered by a plastic *sock*, were placed for a rapid saturation of the bentonite using an artificial groundwater (Table 2). The initial water content of the compacted bentonite was that of "as-received" air dried material. The dry density of the blocks installed in 2013 can be seen in Table 3.

The ABM45 experiments were sparsely instrumented (Figure 1). Only twenty thermocouples type T (Chromel-alumel with a shield of cupronickel, 4.5 mm diameter) were installed in blocks numbers 3, 9, 15, 21 and 27. Four thermocouples were installed at each level in pre-drilled holes in the bentonite rings, one on the steel surface and three in the buffer at a radial distance from the heater (5, 40 and 60 mm). In addition, 8 copper specimens (10 mm diameter, 25 mm height, Cu-OFP: oxygen-free phosphorous doped) and 8 titanium specimens (tube of 6 mm outer and 4 mm inner diameters) were positioned. The specimens were installed on the surface in pre-drilled holes followed by a small bentonite cylinder (Figure 1). The copper specimens were positioned in blocks 16 and 20 at 3 cm distance from the heater in four directions (0°, 90°, 180° and 270°). In the case of Titanium specimens, four of them were installed in each of the two chosen blocks (#3 and #15), inside holes drilled mid-height of the block periphery in four directions (0°, 90°, 180° and 270°).

The dismantling operation of the ABM5 experiment began on last June 2017. Some blocks looked rather intact while others were highly fractured and very fragile due to the high temperature. Different bentonite samples were obtained for performing various studies by different laboratories (e.g., [3-5]. Most of the bentonite samples were wrapped and preserved inside vacuum-sealed aluminium-foil bags. It was intended that the sam-

ples were retrieved and collected with minimal exposure to the atmosphere (few hours) before packing.

Table 1. Chemical composition in wt.% of carbon steel (steel grade P235TR1, 1.0254): EN 10216-1-2014.

Element	Fe	C	Si	Mn	P	S	Cr	Mo	Ni	Cu	Nb	Ti	V
maximum	ball	0.16	0.35	1.20	0.025	0.02	0.30	0.08	0.30	0.30	0.01	0.04	0.02

Table 2. Main composition of the Äspö Groundwater from water supply borehole KA2598A [1].

Ion	Water-type	I (M)	Na	K	Ca	Mg	HCO_3^-	Cl^-	SO_4^{2-}	Br^-	F^-	Si	pH
mg/L	Ca-Na-Cl	0.91	2470	12.4	2560	64.8	51.7	8580	483	59	1.5	6.3	7.33

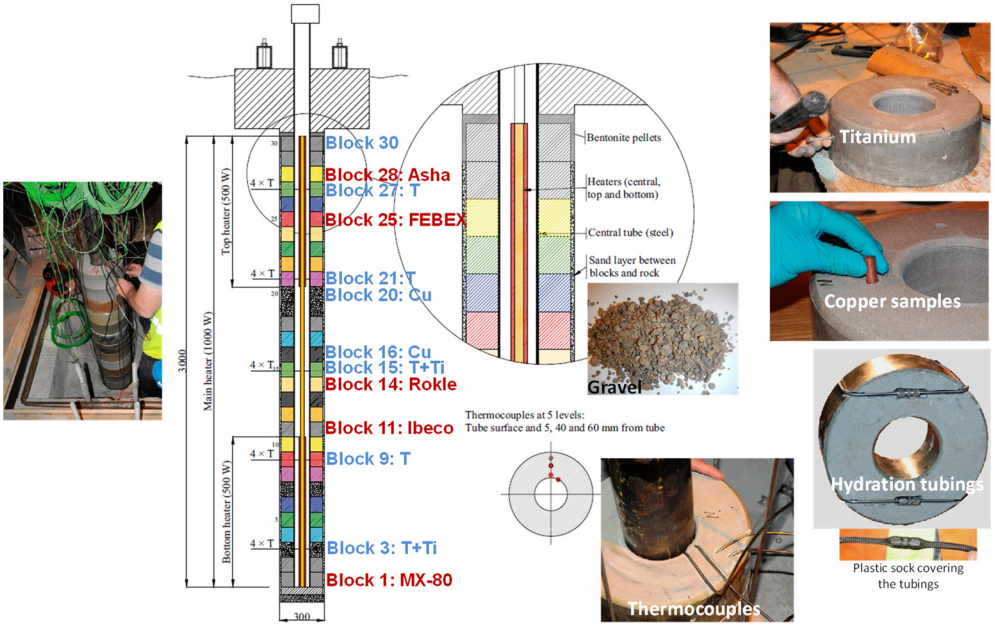

Figure 1. Schematic design of the ABM 5 test package (after [2]). In red: samples analysed in this study. In blue: block containing thermocouples and Cu and Ti coupons.

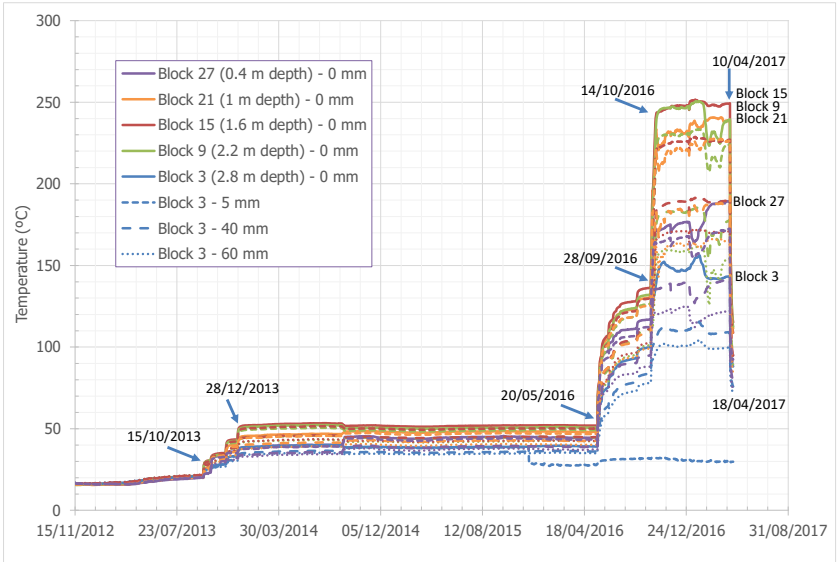

Figure 2. Temperatures profiles as a function of the heater contact (0, 5, 40 ad 60 mm) measured by thermocouples inside bentonite blocks nº 3, 9 (Asha NW BFL-L), 15 (MX-80), 21 (Kunigel) and 27 (Calcigel).

2.2. Materials

For this study, four slices from bentonite samples collected after dismantling were sent to CIEMAT in June 2019 (Figure 1): MX-80 from block position 1 (3 m depth), Ibeco from block position 11 (2 m depth), Rokle from block 14 (1.7 m depth), FEBEX from block position 25 (0.6 m depth), and Asha 505 from block position 28 (0.3 m depth). These bentonites correspond to mainly Na- and Ca-Mg-smectites [6].

MX-80 bentonite is known as Wyoming bentonite coming from USA. This bentonite is composed by a sodium montmorillonite (~82-84 wt.%) that occurs as layers in marine shales, and is widespread and extensively mined, not only in Wyoming but also in parts of Montana and South Dakota. The bentonite formed through alteration of rhyolitic tephra deposited in ancient Mowry Sea basin during the Cretaceous, more than 65 million years ago [7].

IBECO Deponit-CA-N is a Greek bentonite, quarried by S&B Industrial Minerals, S.A. in the north-eastern part of the island of Milos. Pyroclastic tuffs and lavas of andesitic to dacitic composition are the main parent rocks of this bentonite, which forms irregular bodies with a thickness of 10–40 m within the pyroclastics. The bentonite formation is a result of hydrothermal reactions between the permeable volcanic rocks and percolating groundwater heated to below 90°C during volcanic activity, although there is some disagreement about the genesis, e.g. [8]. The major mineral phase (80-84 wt.%) is calcium montmorillonite.

Rokle bentonite originates from the Rokle deposit in the Kadan basin within the north Bohemian volcanic areas c. 100 km WNW of Prague (Czech Republic). The deposit is part of a series of argillised volcanoclastic accumulations of Tertiary age, formed by auto-hydrothermal alteration in shallow lacustrine basins within the stratovolcano complex of Doupovské Mountains. The bentonite is capped by basaltic lava-flows. The lens-shaped bentonite body has a maximum thickness of c. 40 m and contains more than 40 million tons of bentonite. The volcanic glass is completely altered to smectite, but mm-sized flakes of biotite, which is a primary constituent of the basaltic magma, are relatively frequent. The bentonite is highly variable in colour, ranging from olive-grey to yellow/red due to the admixture of secondary iron and manganese oxides [9,10]. The major mineral phase (~70 wt.%) is calcium montmorillonite, containing also some kaolinite.

FEBEX bentonite was extracted from the Cortijo de Archidona deposit (Serrata de Níjar, Almería, Spain). In this zone, the bentonite deposits are usually associated with fractures, the origin being related to hydrothermal alteration processes that took place in tuffaceous volcanic rocks 15-5 Ma ago (Miocene age). The major mineral phase (90-92 %) is a Ca-Mg-montmorillonite, predominantly calcium [11,12].

Asha 505 is the commercial name of extensive deposits of natural Na-bentonite quarried in the Kutch area, 60-80 Km from the ports of Kandla and Mandvi on the north-west-coast of India. The bentonite is associated with the basaltic Deccan Trap rocks of Tertiary age and formed through hydrothermal alteration of volcanic ash in saline water [13]. The bentonite occurs in scattered pockets or layers within the basaltic rocks, with thicknesses ranging between few to 30 meters. The major mineral phase (80-87 wt.%) is sodium montmorillonite, also containing some kaolinite. Because of the high content of secondary iron oxides, the color is normally dark reddish brown.

At laboratory, the received portion of each ring-shaped bentonite block was sampled along one radius. The samples were sliced with a knife in several parts from the granite contact towards the heater contact. Several subsamples were used for different analyses (Figure 3).

2.3. Methods

The objective of the laboratory tests was to undertake a comprehensive analysis of the blocks in order to determine the physical, physico-chemical, mineralogical and geo-

chemical characteristics of the buffer for the assessment of the properties of the bentonite material after the heating and hydration process over 4.4 years of experiment.

2.3.1. Physical properties

The gravimetric water content, *w.c.*, is defined as the ratio between the weight of water and the weight of dry solid expressed as a percentage. The weight of water was determined as the difference between the weight of the sample and its weight after oven drying at 110°C for 48 hours (weight of solid).

Dry density, ρ_d, is defined as the ratio between the weight of the dry sample and the volume occupied by it prior to drying. The volume of the specimens was determined by immersing them in a recipient containing mercury and by weighing the mercury displaced, as established in UNE Standard 7045 "Determination of soil porosity".

Figure 3. Sampling of the bentonites at laboratory for performing different analyses.

2.3.2. Mineralogical analysis

XRD diffraction patterns were obtained from random powders and oriented aggregates. The bulk sample powders were obtained by grinding the samples in a RETSCH RM 100 mortar grinder with a pestle of agate to a size of less than 63 μm after drying them at ambient temperature. The powders were analysed with a Philips X'Pert –PRO MPD diffractometer, using an anticathode Cu-K_α at 45 kV and 40 mA, equipped with a fixed divergence slit (0.1245° size), Scientific X´celerator detector. The samples were investigated from 2° to 70° 2θ with a step size of 0.017° 2θ , and a scan rate of 50 s per step for the powder samples. Mineral identification and quantitative analyses were performed by using the HighScore program v.5 and the Power Diffraction File database from the International Center for Diffraction Data (ICDD).

The modified Jackson treatment [14] was used to separate the clay minerals from the rock matrix [15]. The fine fraction of less than 2 μm was obtained by suspension and sedimentation in deionised water. The final clay suspension was ultrasonic dispersed using 1 g in 5 mL of deionized water. Oriented mounts were prepared by suction of the dispersion through 3 mm thick ceramic tiles by applying vacuum. These clay films (air dried, ethylene glycol solvated and 550 °C heated) were X-rayed from 2 to 35° 2θ using a Bruker D8 Advance diffractometer with an anticathode Cu-Kα at 40 kV and 30 mA, equipped with a fixed divergence slit (0.15° size). The samples were investigated a step size of 0.02° 2θ, and a scan rate of 2 seconds per step.

Fourier Transform Infrared (FTIR) spectroscopy is complementary to X-ray diffraction and other methods. Fourier transform IR spectra were obtained in the middle-IR region (4000-400 cm^{-1}) with a Nicolet iS50 with a DTGS KBr detector (resolution 4 cm^{-1}, 32 scans) on KBr-pressed discs in transmission technique in an atmosphere continuously purged from water and atmospheric CO_2. Two milligrams of powdered air-dried sample were dispersed in 200 mg of KBr and pressed to a clear disc. The pressed samples were analysed at room temperature and then after heating in an oven overnight at 110°C.

Scanning electron microscopy (SEM). A JEOL JSM-820 SEM microscope coupled to a X Oxford ISIS Link energy dispersive X-ray energy spectrometer (XEDS), which allows for the qualitative analysis of light elements from boron, were used to define the microstructural morphology of clay minerals, possible alteration products and accessory minerals. Most of the clay samples were dried at 40-60°C in an oven overnight, and then subjected to a gold metallization by applying $5 \cdot 10^{-2}$ Torr vacuum and a gold coating of 300 to 400 Å thickness, using a BALZERS SCD 004 sputter coater for the scanning electron microscopy analysis. The composition of dioctahedral smectites and illites was calculated using the structural formula method according to [15,16], on the basis of 11 oxygen atoms equivalent per half unit cell (e.phuc^{-1}), tetrahedral occupation by 4.0 cations ($^{IV}Si+^{VI}Al$), octahedral occupation by 2 cations, and complete oxygen/hydroxyl framework of $O_{10}(OH)_2$. For chlorites […$O_{10}(OH)_2$-1H_2O] and kaolinites […$O_5(OH)_4$-1H_2O], 14 and 7 oxygen atoms e.phuc^{-1} were used, respectively.

XPS. X-ray Photoelectron spectroscopy (XPS) data were recorded using a Phoibos-150 electron analyser (SPECS) under a pressure lower than $2 \cdot 10^{-9}$ mbar using Al Kα radiation. The wide scan spectra and the narrow (high resolution) spectra were recorded using a constant pass energy of 100 and 20 eV, respectively. The binding energy (BE) scale was referenced to the BE of the main C-C contribution (284.6 eV) of the C 1s spectrum corresponding to the adventitious contamination layer. All the spectra were computer-fitted using pseudo-Voight line profiles and the CASAXPS software. Relative atomic concentrations were calculated by peak integration after background subtraction using the Shirley method and the atomic sensitivity factors tabulated by Wagner [17].

Mössbauer spectroscopy. ^{57}Fe Mössbauer spectroscopy data were recorded at room temperature (300 K) in transmission mode using a conventional constant acceleration spectrometer and a ^{57}Co (Rh) source. Absorbers were prepared to have an effective thickness of about 5-10 mg of natural iron per square centimeter. The velocity scale was calibrated using a 6 μm thick natural iron foil. All the spectra were computer-fitted using

Lorentzian lines and the isomer shifts were referred to the centroid of the α-Fe sextet at room temperature.

2.3.3. Geochemical analysis

2.3.3.1. Chemical composition by X-ray Fluorescence

The major elements (SiO_2, Al_2O_3, Fe_2O_3, MnO, MgO, CaO, Na_2O, K_2O, TiO_2, P_2O_5 and SO_3 in %) were analysed by X-Ray Fluorescence Analysis (XRF) in natural powdered samples, which were ground to < 250 μm. The XRF analyses were performed on an Axios spectrometer from Panalytical equipped with a rhodium X-ray tube (stimulation power: 1 KW). The dissolution or decomposition of the sample into a homogeneous glass was obtained by fusion, which consisted in heating a mixture of sample and flux ($Li_2B_4O_7$) at high temperatures (800 to 1000°C) so that the flux melts and the sample dissolves. The end-product after cooling is a one-phase glass.

Powdered samples (0.8 g of oven-dried samples at 105°C) were homogeneously mixed with 7.2 g of lithium tetraborate in the proportion of 34-66%. The whole material was molten stepwise in a platinum crucible at a smelting apparatus. After this procedure, the melt was transferred into a platinum jacket and cooled. The loss of ignition was determined separately by oven-drying the dried sample at 1025°C for 3 hours.

2.3.3.2. Chemical Total Carbon and Total Sulfur

Total Carbon, total sulfur and total inorganic carbon were determined on 0.2 g of powdered solid samples obtained from a representative and homogeneous sample. The powders were obtained by grinding the air-dried samples in a RETSCH RM 100 mortar grinder with a pestle of agate to a size of less than 250 μm. Total Carbon (TC) and Total Sulfur content were determined on the solid sample by means of a LECO CS-244 analyzer by combustion. The total inorganic carbon (TIC) content was obtained with a TOC-V_{CSH} analyzer (SHIMADZU, Shimadzu Scientific Instruments, Kyoto, Japan) equipped with a SSM-5000A module. The presence of organic carbon was evaluated by the difference between TC and TIC.

2.3.3.3. Chemical Fe(II)-Fe_{total} in the samples

Fe(III) and Fe(II) were leached from the samples by using a modification of the procedure described in [18] and analysed by 1,10 phenanthroline spectrophotometric method. To a finely ground sample of 0.1-0.2 g, 1 g of NH_4HF_2 and 10 mL of 1:1 H_2SO_4 were added to a 40 mL high-density polyethylene (HDPE) tubes. The tubes were closed with caps and heated to 90°C for 60 minutes in a shaking water bath. After this extraction process, the tubes were allowed to cool to room temperature. The contents were transferred to 50-100 mL volumetric flasks and made up to volume with MilliQ water. For the spectrophotometric determination of Fe(II), a 1-5 mL aliquot (duplicate) was taken in a 50 mL volumetric flask; 5 mL of 6 M sodium acetate and 1 mL of 1% 1.10 phenanthroline were added, mixed well and made up to volume with MilliQ water. After 15 minutes, the absorbance at 510 nm was measured against a blank of reagents. For the spectrophotometric determination of total-Fe, another aliquot (duplicate) was taken in a separate 50 mL volumetric flask and 2 mL of 10% hydroxylammonium chloride were added to it. This was mixed well and was allowed to stand 20 min. Then, 5 mL of 6 M sodium acetate and 1 mL of 1% 1.10 phenanthroline were added, mixed well and made up to volume with MilliQ water. After 15 minutes, the absorbance at 510 nm was measured against a blank of reagents. The contents of iron were determined in the samples from the calibration curve prepared from iron standard solutions. The estimation of ferric iron was made by subtracting the ferrous iron content from the total iron content.

2.3.4. Physico-Chemical Characterization

2.3.4.1. Cation Exchange Capacity

Total CEC was measured with 0.01 M copper triethylenetetramine, Cu-Trien or $[Cu(Trien)]^{2+}$, solution [19]. 200 mg of air-dried clay sample were weighed in 60 mL centrifuge tubes. 25 mL of deionized water were added, and the suspension was dispersed

by ultrasonic treatment for 5 min. Then, 10 mL of 0.01 M $[Cu(Trien)]^{2+}$ were added and allowed to react by end-over-end shaking for 1 hour. After this procedure, a complete exchange of the $[Cu(Trien)]^{2+}$ complex with the exchangeable cations is guaranteed. Afterwards, the suspensions were centrifuged at a constant rotation speed of 11000 rpm for 30 min. 3 mL of the clear blue solution (filtered through 0.45 μm pore size syringe filter) were filled into 1 cm optical glass cuvettes and the absorbance of the solution was measured at 578 nm wavelength by using a Merck spectrophotometer. The analyses were performed on duplicate. The standard deviation of the measurement is ±2 meq/100g.

2.3.4.2. Cation Exchange Population

The determination of the cation exchange population was performed by using Cs as index cation [20]. Caesium acts as a highly selective cation to displace all exchangeable cations from the clay minerals if its concentration is sufficiently high. Solid air-dried samples were equilibrated inside a JACOMEX glove box (< 1 ppm O_2) at 1:4 solid to liquid ratio (0.25 kg/L) with 0.5 M $CsNO_3$ at pH 8.2. After phase separation by centrifugation (1100 rpm, 30 min., outside the glove box), the supernatant solutions were filtered through 0.2 μm pore size syringe filter (inside the anoxic glove box), and the concentration of the major cations was analysed. Sodium and calcium content was corrected with respect to soluble salts.

2.3.4.3. BET External and Total Surface Area

Classical nitrogen adsorption/desorption isotherms were obtained on a discontinuous volumetric sorptometer, Micromeritics ASAP 2020 V3.02 H. Approximately 0.5 grams of total sample were ground in an agate mortar. The samples were dried at 90°C during at least 24 h before the tests. Prior to the nitrogen adsorption, the samples were out-gassed by heating at 90°C for 18 hours using a mixture of helium and nitrogen under a residual vacuum between 500 and 6-10 μmmHg. The tests were performed at the boiling point of liquid nitrogen (77 K) considering a molecular cross section area of 0.162 nm2 for the nitrogen molecule. External surface areas were calculated using the standard N2-BET method, using a series of data points over the P/P0 range of 0.02 to 0.25 on the nitrogen adsorption isotherm [21].

In contrast to nitrogen, which is only adsorbed at the external surface of the stacks of the layers, water molecules can be adsorbed on the whole surface, including both the internal (interlayer) and external surfaces of the clay minerals. Thus, in order to obtain the Total specific surface area (SA), water vapour gravimetric adsorption measurements were performed by Keeling´s hygroscopic method [22] by storing the samples at a constant 75% relative humidity atmosphere in a chamber over-saturated in NaCl solution for 1 month. Prior to the tests the samples were dried at 110°C during 24 hours. The weight changes of the samples as the adsorbed amount of water were measured and related with the total surface area, SA.

2.3.4.4. Soluble salts by aqueous leaching

The soluble salts have been analysed in aqueous extract solutions. The subsamples were crushed without previous drying, and placed in contact with deionised and degassed water at 1:4 solid to liquid ratio, shaken end-over-end and allowed to react for one day under anoxic conditions inside an anoxic glove box with oxygen content below 1 ppm. After phase separation by centrifugation (30 minutes at 11000 rpm), the supernatant solutions were filtered through a 0.2 μm pore-size syringe filter (inside the anoxic glove box) and analysed.

2.3.5. Pore water Chemistry

The pore water of the bentonite samples was obtained by the squeezing technique at high pressures [23,24,25]. Squeezing is analogous to the natural process of consolidation, caused by the deposition of material during geological time, but at a greatly accelerated rate. The squeezing process involves the expulsion of interstitial fluid from the saturated clayey material being compressed [26].

At CIEMAT the squeezing rig is similar to that developed by [26] and [27]. The squeezer has been designed to allow a one-dimensional compression of the sample by means of an automatic hydraulic ram operating downwards, the squeezed water being expelled from the top and bottom of the cell into a vacuum vial (Figure 3). The compaction chamber is made of type AISI 329 stainless steel (due to its high tensile strength and resistance to corrosion) with an internal diameter of 70 mm. The compaction chamber is 250 mm high with 20 mm wall thickness and allows pressures up to 100 MPa.

The filtration system allows the extraction of interstitial water by drainage at the top and at the bottom of the sample. This system comprises a 0.5 μm stainless steel AISI 316L porous disk (Cr 17.36%, Ni 11.4%, Mo 2.15%, Si 0.94%, Mn 0.17%, C 0.027%, S 0.011%, P 0.022%, Fe 66.92%) in contact with the sample. The liquid is collected through stainless steel tubes ($^1/_{16}$ inch) in a vacuum vial sealed by a septum. The whole system remains under ambient conditions (room temperature of about 22-25 ºC). However, a sampling circuit was designed for collecting the water at anoxic conditions (Figure 4). At the beginning of the test, the squeezing cell and all the samplings tubings and vials were closed to ambient. Then, several cycles of Ar-flusing and vacuum were performed, preserving the system under anoxic conditions.

The bentonite samples for squeezing were prepared using a knife to remove the outer part in order to discard possible material contaminated. The sample was cut in a cylindrical shape, weighed and placed into the body of the cell. A small stress of 1 to 5 MPa was initially applied to remove most of the atmospheric gas from the cell and allow the sample to bed in. After applying two additional Ar-flushing and vacuum cycles to the sampling circuit, the stress was progressively increased up to the selected pressure, rather than in a single step. This avoids overconsolidation or collapse of the clay-pore system. When the maximum of squeezed water was obtained for a given pressure, the vial was removed, keeping the sample away from any contact with the atmosphere. The water sample collected was weighed and immediately analysed. The bentonite mass was also weighed, and the final water content and dry density was determined. During the squeezing test, the evolution of the pressure, axial strain and changes in the length of the sample due to consolidation were recorded over time by using a data acquisition system. The chemical analysis of the water samples was performed with the methods described in Section 2.3.6.

2.3.6. Water chemical analyses

The water samples were filtered through 0.2 μm syringe filters, except those for pH and electrical conductivity (EC) measurements. The pH was measured by means of an ORION 720A pH-meter equipped with a Metrohm 6.0224.100 combined pH micro-electrode. Merck pH buffer solutions of pH 4.0 and 7.0 were used for pH-meter calibration. The total *alkalinity* of the water samples was determined with a specific Dynamic Equivalence Point Titration (DET) method for analysing samples of 1-2 mL. The instrumentation consists of a Metrohm 888 Titrando equipment with a 5 mL burette and a 6.0224.100 Metrohm combined pH micro-electrode. The *major and trace cations, including silica,* were analysed by Inductively Coupled Plasma Optical Emission Spectrometry (ICP-OES) in a Varian 735ES spectrometer. Sodium and potassium were determined by atomic absorption spectrometry in an Agilent AA 240 FS spectrometer. A*nions* were analysed by ion chromatography (Dionex ICS-2000).

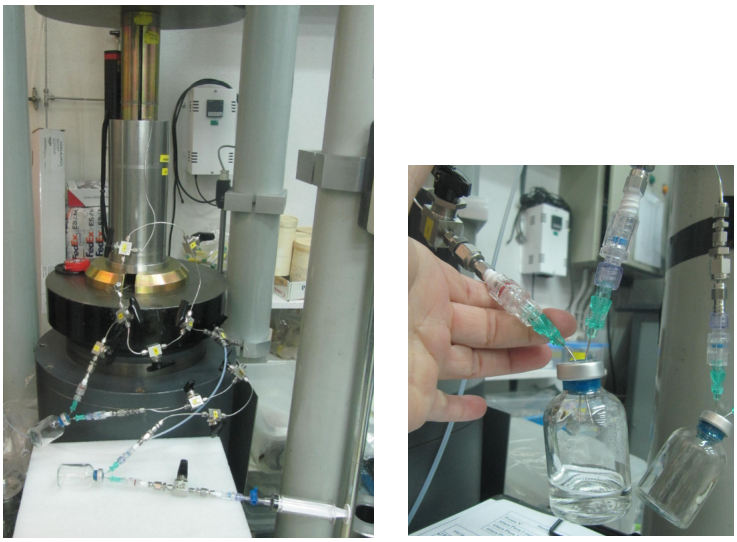

Figure 4. Sampling of the bentonites at laboratory for performing different analyses.

3. Results

3.1. Physical properties

The characteristics of the bentonite blocks at initial conditions before the *in situ* experiment are given in Table 3 and Table 4. The initial water content is between 10.6 to 17.2%, the dry density between 1.80 to 1.93 g/cm^3 and the degree of saturation between 67 to 84%. After 4.4 years of artificial hydration and heating, the samples increased their water content up to ~30 ± 2%, showing lower values towards the heater contact. The dry density decreased up to ~1.52 ± 0.05 g/cm^3, with a tendency to increase at heater contact (Table 4). It is interesting to note that although complete saturation was achieved, the degree of saturation increased from the top to the bottom of the bentonite package (from 93 to 100% of saturation), as described in [3], probably due to gravity, the highest temperatures at the central part and to steam-bentonite interactions at the top of the bentonite package (Figure 2).

3.2. Mineralogy

3.2.1. XRD Analysis

The random powder patterns of the samples analysed shows the strongest (001) reflection of smectite located at ~14-15Å indicative of a two-layer hydrate Ca-Mg-Montmorillonite (Figure S1 from Supplementary Data, Figure 5). This is due to the saline Na-Ca-Cl-groundwater/bentonite interactions which provoked cation exchange reactions. Na-bentonites (MX-80 and Asha 505) have changed the character of the smectite particles acquiring a Ca-character, shifting d(001) values from 12 Å to 15 Å. In turn, the initial Ca-bentonites (FEBEX, IBECO, Rokle) reveals two populations of water-hydrated montmorillonite clay particles, increasing the one-layer hydrate Na-montmorillonite component (~12 Å). None of the bentonites showed significant indication of any smectite loss or transformation.

d(006) XRD reflexion was centered at 1.49-150 Å both in reference and retrieved samples, no changes being observed even in the samples located at heater contact (Figure 5). This indicates that the presence of new formed trioctahedral smectites (saponite), appearing at 60-61 °2θ, can be ruled out after experiment, in contrast to former ABM experiments [1,29, 30] or in other *in situ* experiment, such as FEBEX *in situ* test [31].

XRD analyses of oriented aggregates were analysed to verify possible changes in clay mineral particles, increasing Ilt/Sme interstratified and/or mixed-layered clay minerals after the high temperature heating experiment. However, no significant differences are observed in the oriented aggregates (Figure 6, Figure S2 from Supplementary Mate-

ria). The dioctahedral smectites preserve their expandability (i.e., no illitization), according to the (001) reflexion around 17Å in the EG XRD pattern for all samples, which indicates complete expansion of the interlayer sites. Kaolinite was present in the reference sample of Asha 505 bentonite and it is not a neoformed clay mineral.

Table 3. Average physical properties from bentonite blocks analysed at CIEMAT prior (initial) and after 4.4 years of test (final).

Sample	Depth (m)	Max. temp. (°)[4]	Bentonite mass (g)	Water content w.c. (%)		Dry density (g/cm³)		Grain Density (g/cm³)[2]	Porosity (%)		Degree of Saturation (%)		Water content at Saturation (%)
			Initial[1]	Initial[1]	Final[3]	Initial[1]	Final[3]		Initial	Final	Initial	Final	Final
Asha Block 28	0.3	187.0	10820	13.1	30.1	1.84	1.49	2.869	36	48	67.3	93.0	32.4
FEBEX Block 25	0.6	216.5	10640	14.3	27.9	1.80	1.51	2.735	34	45	75.2	94.1	29.7
Rokle Block 14	1.7	252.6	10800	17.2	29.0	1.80	1.60	2.940	39	46	80.3	102.2	28.4
IBECO Block 11	2.0	255.1	10740	14.7	32.0	1.86	1.50	2.753	33	45	83.6	106.0	30.2
MX-80 Block 1	3.0	155.0	11040	10.6	31.1	1.93	1.49	2.735	29	46	69.9	101.7	30.6

[1][2]; [2][1]; [3]Average values; [4]Estimated from thermocouples measurements

Table 4. Physical properties of bentonite blocks analysed as a function of the heater contact (see locations in Figure 3).

Subsample	Distance to heater (cm)	Water content w.c. (%)	Grain Density (g/cm³)[1]	Dry density (g/cm³)	Porosity (%)	Degree of Saturation (%)
Asha Block 28 granite (G)	8.33	30.3	2.869	1.49	0.48	93
Asha Block 28 central (M)	5.00	29.9	2.869	1.49	0.48	92
FEBEX Block 25 granite (G)	8.33	28.1	2.735	1.51	0.45	94
FEBEX Block 25 central (M)	5.00	27.8	2.735	1.51	0.45	94
Rokle Block 14 granite (G)	8.33	29.9	2.940	1.63	0.45	109
Rokle Block 14 central (M)	5.00	28.2	2.940	1.58	0.46	96
IBECO Block 11 granite (G)	8.33	33.1	2.753	1.44	0.48	100
IBECO Block 11 heater (H)	1.67	30.9	2.753	1.56	0.43	112
MX-80 Block 1 granite (G)	8.33	32.5	2.735	1.46	0.47	102
MX-80 Block 1 heater (H)	1.67	29.8	2.735	1.52	0.45	101

[1][1].

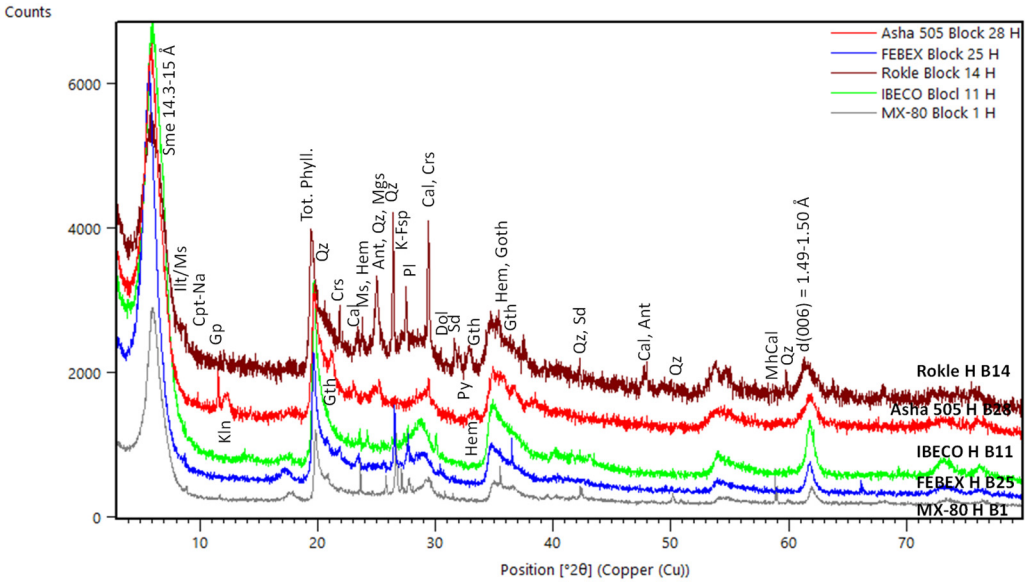

Figure 5. XRD patterns of bulk samples from ABM5 experiment. Symbols according to [28]. Sme: smectite, Ilt/Ms: illite/muscovite, Cpt-Na: Clinoptilolite, Gp: Gypsum, Tot. Phyll: total phyllosilicates, Crs: cristobalite, Cal: calcite, MhCal: monohydrocalcite, Qz: quartz, K-Fsp: potassium feldspar, Pl: Plagioclase, Dol: dolomite, Gth: goethite, Hem: hematite.

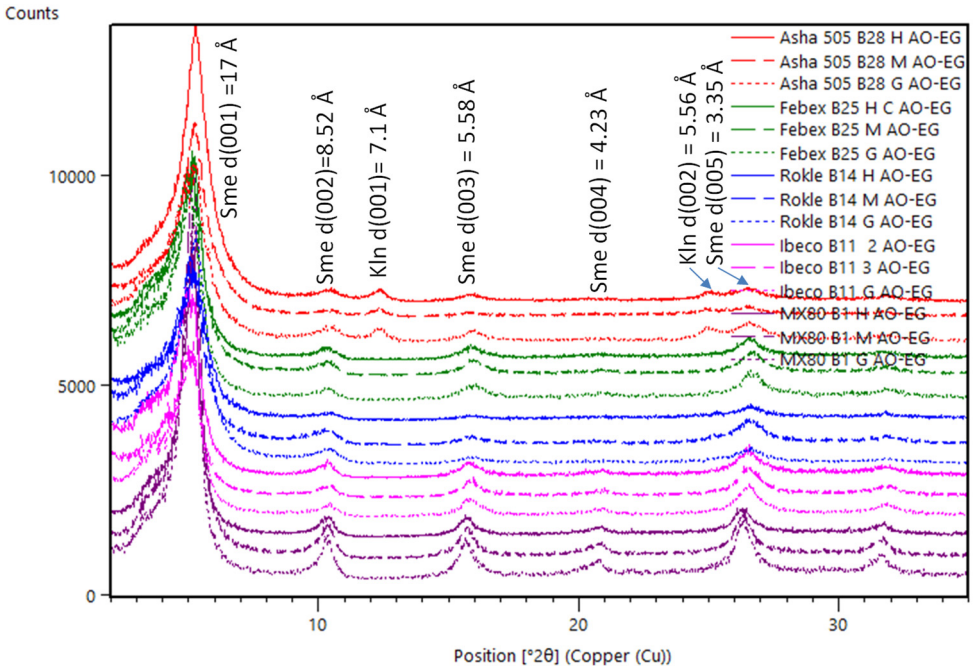

Figure 6. XRD patterns of oriented aggregate samples (after ethylene glycol treatment).

Regarding other accessory mineral phases (Figure S1 from Supplementary Material and Figure 5), Asha 505 bentonite block 28 showed the highest mineralogical differences in the sample at contact with the heater interface, in which gypsum, Na-clinoptilolite and an increase of calcite and Fe-oxides (goethite, hematite) were observed. FEBEX bentonite block 25 shows an increase of calcite, feldspars and presence of gothite (Figure S1). Rokle bentonite block 14 increased the amount of goethite, hematite, calcite, dolomite and presence of siderite. IBECO bentonite block 11 showed similar patterns to original bentonite sample, except the absence of calcite. MX-80 bentonite block 1 shows increased amounts of calcite, gypsum, goethite and hematite and presence of monohydrocalcite, siderite and pyrite.

3.2.2. FTIR analysis

The bentonite samples were also analysed by FTIR for acquiring information of possible changes in the smectite structure, chemical composition and surface properties due to chemical modifications; as well as to investigate mineral neoformations.

The spectra from the bulk samples of different bentonite blocks as a function of heater contact are shown in Figure 7 and 8. All spectra contain the main typical dioctahedral smectite bands (Table S2 from Supplementary Material). The spectra show a band at 3627 cm^{-1} which corresponds to the typical OH stretching region of structural hydroxyl groups for dioctahedral smectites with Al-rich octahedral sheets. These are inner hydroxyl groups lying between the tetrahedral and octahedral sheets. The broad band near 3426 cm^{-1} is due to stretching H-O-H vibrations of adsorbed water, while the band at 1642 cm^{-1} corresponds to the OH deformation or bending adsorption of water. However, additional bands around 3697 cm^{-1} indicate the presence of kaolinite in the Asha 505 and Rokle samples, initially present in the raw samples. If the Si-O absorptions and OH bending bands in the 1300-400 cm^{-1} range are examined, only one broad, complex Si-O stretching vibration band at around 1030 cm^{-1} is seen, which is typical of dioctahedral montmorillonite. In this range, the occupancy of the octahedral sheet can be distinguished due to each cation strongly influences the position of the OH bending bands, which arise from vibrations of the inner and surface OH groups. In all samples the

presence of a peak at 915 cm^{-1} (δAlAlOH) is observed, which typical of dioctahedral smectites. All samples from bentonites Febex, Ibeco and MX-80 show a band at ~840 cm^{-1} (δAlMgOH), indicating a partial substitution of octahedral Al by Mg. Asha 505, Rokle and MX-80 samples reflect an additional partial substitution of aluminium by iron (δAlFeOH), with the band at 874-885 cm^{-1}. However, the Fe substitution of is much higher in Asha 505 samples due to the decrease of the δAlMgOH peak and the increase of the δAlFeOH peak. The adsorption band at 622 cm^{-1} can be attributed to a R-O-Si vibrations (R=Al, Fe, Mg) in smectites and indicates a perpendicular vibration of the octahedral cations and their connection to the tetrahedral sheet. The bands at 520 cm^{-1} and 466 cm^{-1} correspond to Si-O-Al vibration of aluminium in the tetrahedral sheet and Si-O-Si bending vibrations, respectively. All samples show the weak band at 798 cm^{-1} caused by the Si-O stretching of quartz. Calcite (~1426 cm^{-1}) is observed in Asha 505, Rokle, Ibeco and MX-80 samples. However, this peak disappears in all the analysed retrieved samples from the Ibeco bentonite block 11, as seen in XDR patterns, indicating a high mineral dissolution process in this part of the bentonite package. No other alterations are observed between the initial and retrieved samples from the bentonite blocks analysed.

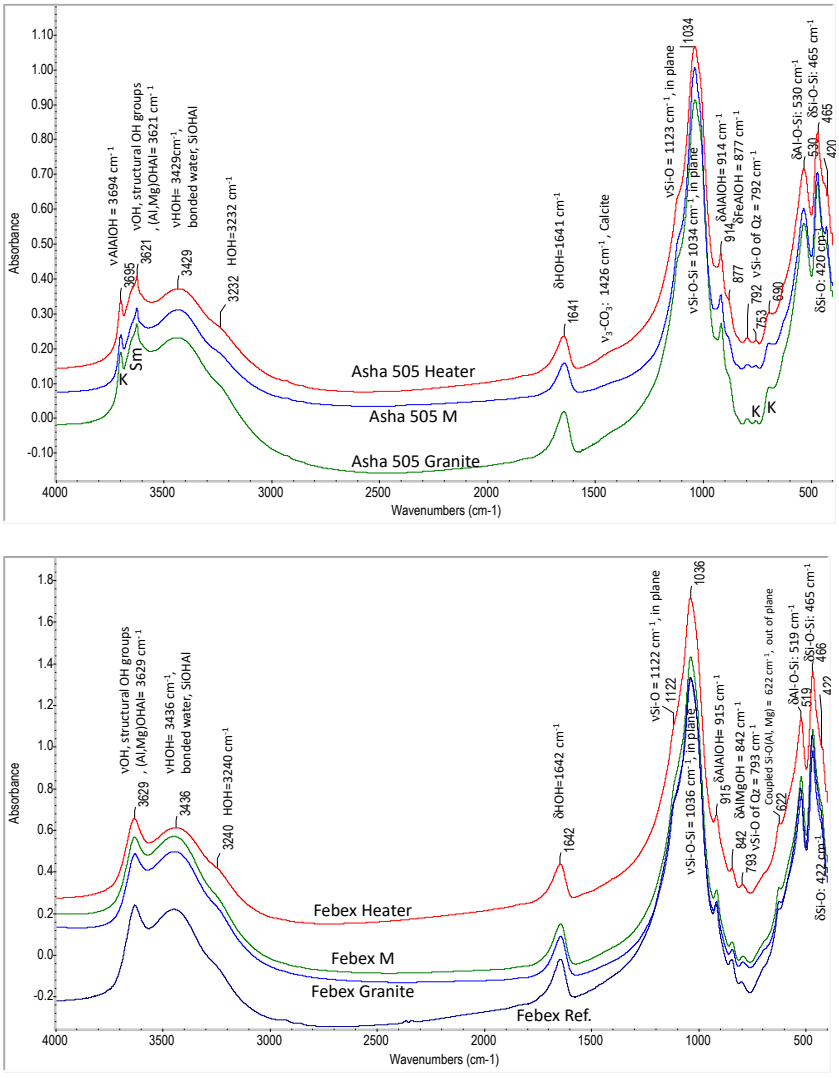

Figure 7. FTIR spectra (OH-stretching and OH-bending regions) from samples taken from the ABM5 experiment: Asha 505 block 28 and Febex block 25.

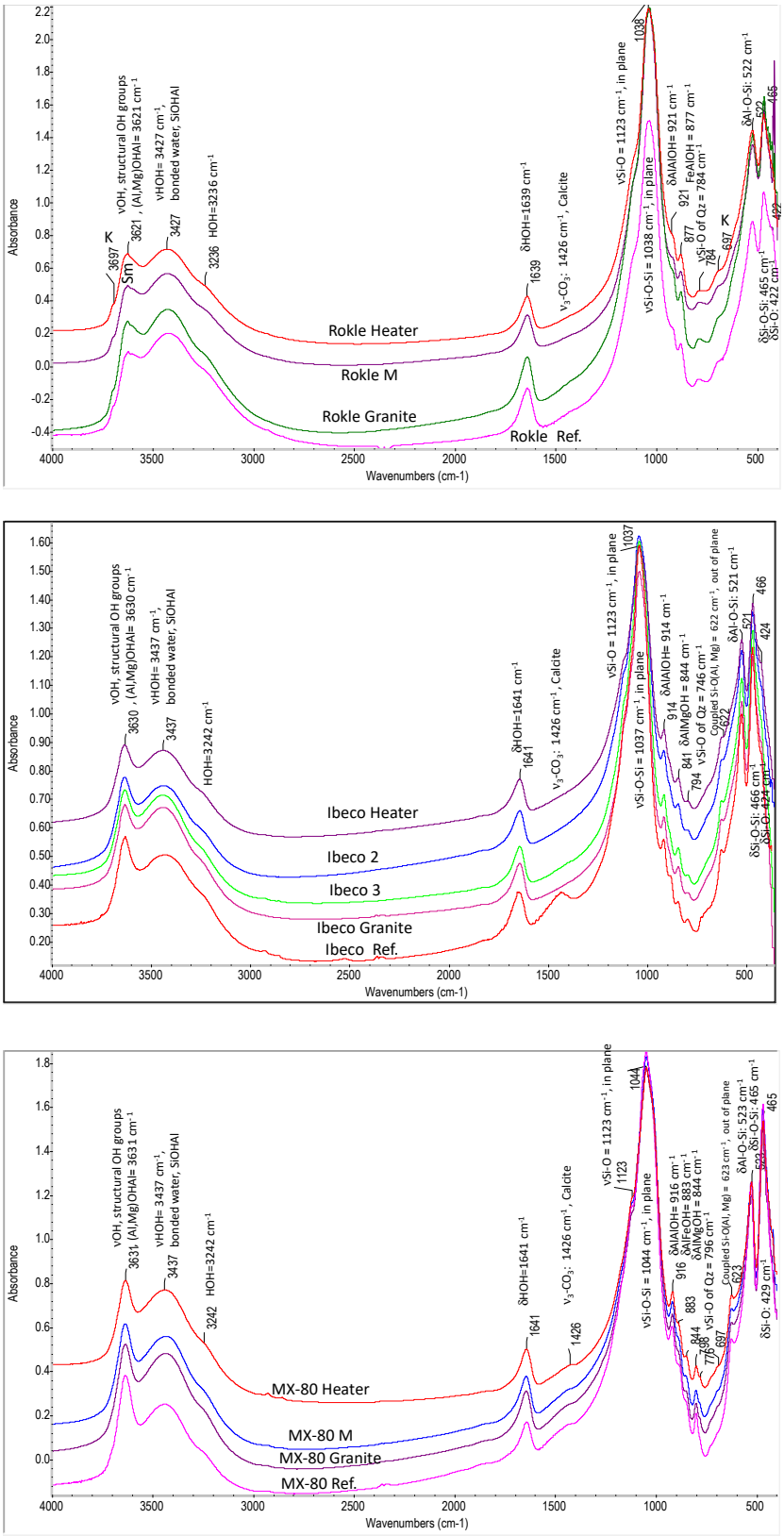

Figure 8. FTIR spectra (OH-stretching and OH-bending regions) from samples taken from the ABM5 experiment: Rokle block 14, Ibeco block 11 and MX-80 Block 1.

3.2.3. SEM Analysis

Bentonite samples at direct contact with the heater were analysed by SEM. All of them showed Fe-hydro/oxides pointing the presence of corrosion products near the heater. Barite was found in FEBEX and Rokle samples and pyrite (FeS_2) and sphalerite (ZnS) in MX-80 samples. All the samples contained in some parts increased of organic carbon (Asha 505, FEBEX, Ibeco). Microbes of fungi type found in FEBEX, Rokle, Ibeco samples (Figure 9) may be formed after dismantling during storage due to the high water content of the samples.

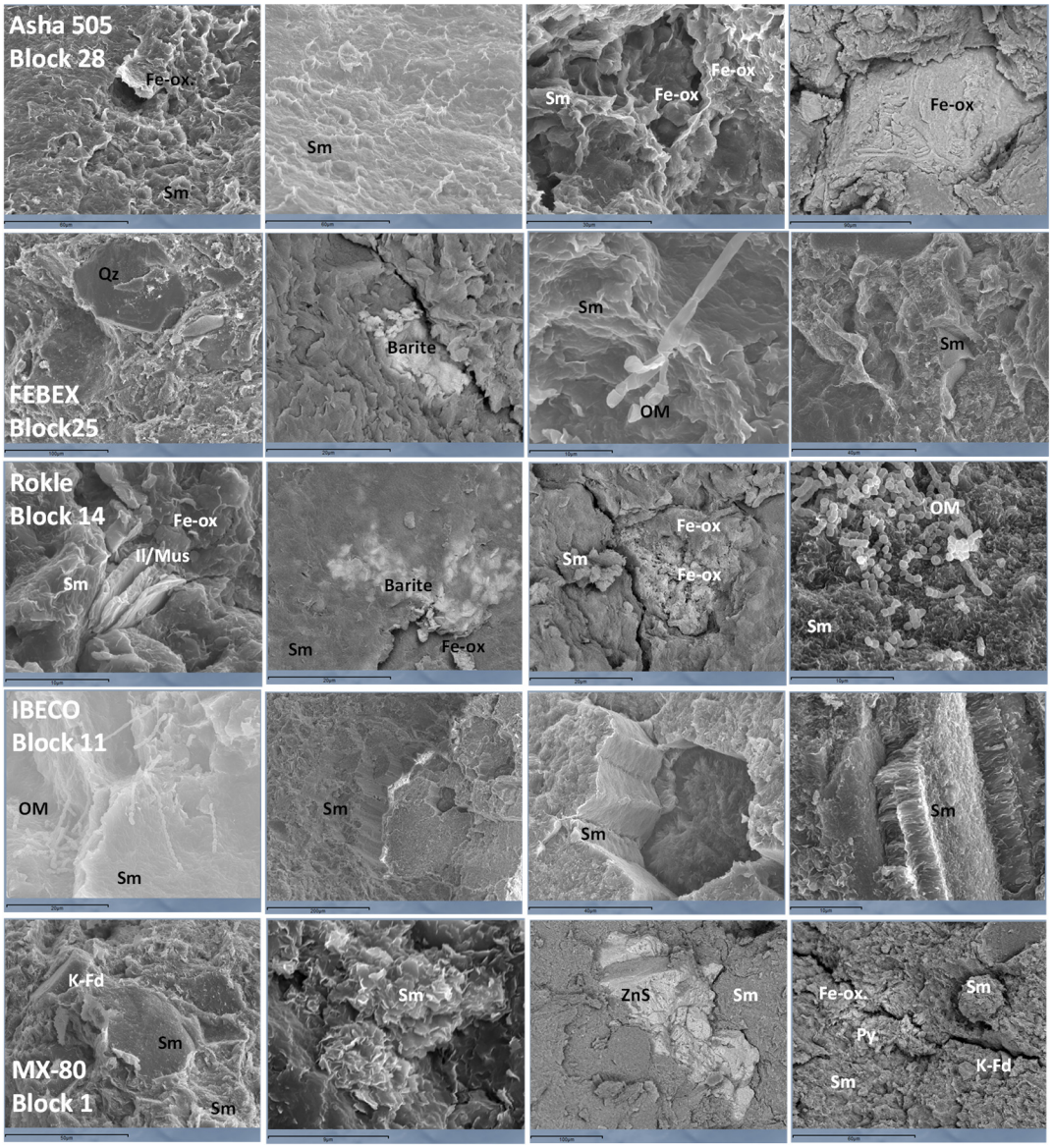

Figure 9. SEM photomicrographs from different bentonites at direct contact with the heater.

The microstructure and composition of the clay mineral particles from samples at contact with the heater contact was analysed by SEM-EDX. The SEM photomicrographs and the crystallochemical formula of the smectite clay minerals analysed are shown in Figure 9 and Table 5. The structure of the clay mineral particles remains intact, showing a porous honeycomb microstructure, following similar patterns observed in original samples prior to the hydration-heating treatment (Figure 9). The clay mineral particles analysed are in the same stability field of the smectite clay mineral as reference samples. However, some particles from deviate from the reference crystallochemical structure, the most significant changes being related to changes in the cation composition at tetrahedral sheets, decreasing tetrahedral silicon, increasing tetrahedral charge and total charge of

the smectite clay particles. This is true except for the Rokle bentonite, in which the excess of charge is located in tetrahedral sheets originally, and after treatment, there is an increase of the octahedral charge, loosing octahedral Al. Fe and Mg content increased at octahedral sheets, but variations are not significant.

Table 5. Structural formula of clay particles analysed in reference samples and close the heater contact.

Sample	Structural formula	Layer charge (eq/h.u.c.)	Σ_{tet}	Σ_{oct}	τ charge (%)	O. charge (%)	Weight (g/mol) p.f.u.
Asha 505 Ref.	$(Si_{3.81}Al_{0.19})^{IV}$ $(Al_{1.28}Fe^{3+}_{0.48}Mg_{0.24})^{VI}$ $O_{10}(OH)_2$ $(Ca_{0.12}Na_{0.21})_{0.32}$	0.43	4.0	*2.00*	44	56	764.87
Asha 505 Block 28	$(Si_{3.81}Al_{0.19})^{IV}$ $(Al_{1.10}Fe^{3+}_{0.74}Mg_{0.16}Ti^{4+}_{0.01})^{VI}$ $O_{10}(OH)_2$ $(Ca_{0.12}Na_{0.05}K_{0.05})_{0.33}$	0.33	4.0	*2.01*	59	41	778.21
	$(Si_{3.84}Al_{0.16})^{IV}$ $(Al_{1.43}Fe^{3+}_{0.32}Mg_{0.23})^{VI}$ $O_{10}(OH)_2$ $(Ca_{0.17}Na_{0.10}K_{0.02})_{0.29}$	0.46	4.0	*1.98*	36	64	756.05
	$(Si_{3.78}Al_{0.22})^{IV}$ $(Al_{1.17}Fe^{3+}_{0.60}Mg_{0.19}Ti^{4+}_{0.01})^{VI}$ $O_{10}(OH)_2$ $(Ca_{0.17}Na_{0.10}K_{0.02})_{0.29}$	0.48	4.0	*1.97*	46	54	772.63
	$(Si_{3.62}Al_{0.68})^{IV}$ $(Al_{0.81}Fe^{3+}_{0.98}Mg_{0.24}Ti^{4+}_{0.004})^{VI}$ $O_{10}(OH)_2$ $(Ca_{0.22}Na_{0.05}K_{0.03})_{0.29}$	0.51	4.0	*2.04*	75	25	798.99
	$(Si_{3.83}Al_{0.17})^{IV}$ $(Al_{1.38}Fe^{3+}_{0.35}Mg_{0.27}Ti^{4+}_{0.03})^{VI}$ $O_{10}(OH)_2$ $(Ca_{0.13}Na_{0.08}K_{0.001})_{0.21}$	0.34	4.0	*2.02*	50	50	755.41
FEBEX Ref.	$(Si_{3.96}Al_{0.04})^{IV}$ $(Al_{1.49}Fe^{3+}_{0.13}Mg_{0.38})^{VI}$ $O_{10}(OH)_2$ $(Mg_{0.10}Na_{0.20}K_{0.03})_{0.32}$	0.42	4.0	2.00	10	90	742.12
FEBEX Block 25	$(Si_{3.96}Al_{0.04})^{IV}$ $(Al_{1.44}Fe^{3+}_{0.12}Mg_{0.43}Ti^{4+}_{0.01})^{VI}$ $O_{10}(OH)_2$ $(Ca_{0.15}Na_{0.13}K_{0.05})_{0.32}$	0.47	4.0	*2.00*	9	91	746.71
	$(Si_{3.72}Al_{0.28})^{IV}$ $(Al_{1.32}Fe^{3+}_{0.39}Mg_{0.26}Ti^{4+}_{0.05})^{VI}$ $O_{10}(OH)_2$ $(Ca_{0.15}Na_{0.11}K_{0.03})_{0.29}$	0.44	4.0	*2.02*	63	37	763.51
Rokle Ref.	$(Si_{3.75}Al_{0.25})^{IV}(Al_{1.19}Fe^{3+}_{0.67}Mg_{0.15}Ti^{4+}_{0.02}Mn^{2+}_{0.01})^{VI}$ $O_{10}(OH)_2$ $(Ca_{0.03}Na_{0.14}K_{0.07})_{0.24}$	0.27	4.0	2.04	93	7	776.00
Rokle Block 14	$(Si_{3.89}Al_{0.11})^{IV}$ $(Al_{0.98}Fe^{3+}_{0.65}Mg_{0.15}Ti^{4+}_{0.08})^{VI}$ $O_{10}(OH)_2$ $(Ca_{0.14}Na_{0.04}K_{0.08})_{0.26}$	0.40	4.0	*1.96*	27	73	777.36
	$(Si_{3.90}Al_{0.10})^{IV}$ $(Al_{0.98}Fe^{3+}_{0.60}Mg_{0.34}Ti^{4+}_{0.06})^{VI}$ $O_{10}(OH)_2$ $(Ca_{0.17}Na_{0.03}K_{0.10})_{0.30}$	0.47	4.0	*1.97*	21	79	776.70
IBECO Ref.	$(Si_{3.96}Al_{0.04})^{IV}$ $(Al_{1.48}Fe^{3+}_{0.20}Mg_{0.37}Ti^{4+}_{0.01})^{VI}$ $O_{10}(OH)_2$ $(Ca_{0.04}Na_{0.09}K_{0.02})_{0.15}$	0.20	4.0	2.07	18	82	743.37
IBECO Block 11	$(Si_{4.0})^{IV}$ $(Al_{1.44}Fe^{3+}_{0.12}Mg_{0.39}Ti^{4+}_{0.04})^{VI}$ $O_{10}(OH)_2$ $(Ca_{0.08}Na_{0.18}K_{0.05})_{0.32}$	0.40	4.0	*1.99*	1	99	745.27
MX-80 Ref.	$(Si_{4.00})^{IV}$ $(Al_{1.51}$ $Fe^{3+}_{0.22}Ti_{0.01}Mg_{0.24})^{VI}$ O_{10} $(OH)_2$ $(Ca_{0.06}Na_{0.15}K_{0.01})$	0.29	4.00	*1.98*	0	100	744.34
MX-80 Block 1	$(Si_{3.77}Al_{0.23})^{IV}$ $(Al_{1.20}Fe^{3+}_{0.60}Mg_{0.17}Ti^{4+}_{0.02})^{VI}$ $O_{10}(OH)_2$ $(Ca_{0.18}Na_{0.04}K_{0.03})_{0.26}$	0.44	4.0	*1.98*	53	47	772.58
	$(Si_{3.92}Al_{0.08})^{IV}$ $(Al_{1.65}Fe^{3+}_{0.14}Mg_{0.26})^{VI}$ $O_{10}(OH)_2$ $(Ca_{0.05}Na_{0.06}K_{0.01})_{0.12}$	0.17	4.0	2.06	48	52	738.05

3.2.4. XPS and Mössbauer Analysis

For analysing the Fe distribution and speciation inside the bentonite block after the *in situ* test, Rokle bentonite was selected due to its high Fe content. Figure S3 from Supplementary Material shows the wide scan XPS spectra recorded from a representative Rokle retrieved sample. The rest of the samples gave very similar spectra. Table 6 collects the atomic percentages obtained from the quantification of such spectra. The atomic concentrations show only minute variations from sample to sample which are within the error of the experimental determination. We must recall that XPS is a surface sensitive technique and, therefore, the quantitative analysis refers to the composition within the characteristic XPS depth probe which is around 3-5 nm.

Table 6. Surface atomic concentrations calculated from the wide scan XPS spectra (in wt.%).

Sample	Fe	O	Ti	Ca	Mg	C	Si	Al
Reference	3.3	52.2	0.7	1.5	3.3	15.4	20.5	3.1
6G	4.4	56.6	0.8	1.3	2.9	11.5	19.5	3.0
5M	4.0	54.7	0.5	1.3	3.2	14.5	15.8	6.0
4H	3.3	53.7	0.9	1.3	3.2	14.8	18.7	4.0

In order to get insight on the surface chemical states of iron and oxygen, high resolution spectra were recorded along the Fe 2p and O 1s spectral regions. The spectra were computer-fitted using previous models [32] and the results are presented in Figure 10. The Fe 2p spectra are all very similar. They are composed by an intense main spin orbit doublet (BE Fe $2p_{3/2}$=712.3 eV; BE Fe $2p_{1/2}$=726.5 eV) and secondary structure: two small shake-up satellites at 722.3 eV and 735.5 eV and a multiplet splitting component at 717.6 eV. These binding energies values and spectral features are all compatible with the presence of Fe^{3+}. It is difficult from these spectra to ascertain if there is any small Fe^{2+} contribution. As it can be observed in Figure S4 of the Supplementary Information it is very complicated to separate in an XPS spectrum small concentrations of Fe^{2+} in the majority presence of Fe^{3+} and vice versa.

The O 1s spectra showed in all the cases four different contributions located at 529.7 eV, 531.5 eV, 532.7 eV and 534.7 eV, which correspond to Metal-O bonds, Al-O bonds, Si-O bonds and organic carbon/adsorbed water, respectively [33, 34, 35, 36]. The spectra show only small differences except for the increase in intensity of the contribution at 532.7 eV along the series. Although this component is mainly due to Si-O bonds, other contributions due to oxygen-containing functional organic groups or chemi-/physisorbed water cannot be discarded either.

Although XPS is a useful technique to determine oxidation states it lacks the specificity of other techniques, such as Mössbauer spectroscopy, to characterize iron compounds. Hence, ^{57}Fe Mössbauer spectroscopy was employed to study the speciation of the Rokle samples. Figure 11 shows the room temperature Mössbauer spectra recorded from these materials.

All the Mössbauer spectra were fitted using six different components whose relative areas varied from sample to sample. Whilst the Reference, 6G (at granite contact) and 5M (at middle bentonite block) samples gave spectra showing the same contributions in different proportions, the sample 4H close to heater contact, gave a quite different spectrum, showing an additional contribution which was not present in the spectra of the other three. Table 7 collects the hyperfine parameters of the different spectral components and Table 8 shows the relative areas of the components obtained from the fit of the spectra.

The spectra of the four samples were dominated by an intense central paramagnetic component which was best-fitted to two different quadrupole doublets (D1 and D2). The hyperfine parameters of these doublets (Table 7) are characteristic of high spin Fe^{3+} in octahedral oxygen coordination [37]. Since for a high spin Fe^{3+} ion (having a half filled $3d^5$ spherically symmetric configuration) the electric field gradient depends only on the lattice charge distribution, a larger quadrupole splitting, Δ, implies a larger distortion from the perfectly symmetrical octahedral coordination [38]. Thus, D1 corresponds to a situa-

tion where the Fe^{3+} is in a lesser distorted octahedral configuration than that represented by doublet D2. These type of quadrupole doublets are very common in the Mössbauer spectra of bentonites. Sometimes they have been interpreted in terms of *cis* and *trans* configurations, associated with the lower and higher Δ, respectively [39,40,41], although some other interpretations consider only that the different Δ values result from different geometrical distortions of the coordination polyhedra and/or to the existence of different ligands beyond the first coordination shell [42,43,44]. The highest paramagnetic contribution corresponds to the Reference sample while the smallest occurs in the 4H sample (close to heater contact).

Apart from these two Fe^{3+} doublets, all the spectra contain a tiny Fe^{2+} doublet, accounting for a 3-4% of the total spectral area. Because of its small intensity and the many overlapping components, its Mössbauer parameters were best determined by recording spectra in a lower range of velocities (Figure S4 from Supplementary Material). As shown in Table 7, these Mössbauer parameters (D3) are compatible with an octahedral high spin Fe^{2+} species [37]. The spectra recorded from the Reference, 6G and 5M samples contain a broad magnetic component which was fitted to two broad sextets, S1 and S2. The Mössbauer parameters of these sextets are compatible with microcrystalline goethite [45]. The occurrence of two different goethite sextets might be due to goethite fractions having different particle size or Al substitution. These goethite contributions increase in the order Reference < 6G < 5M. The spectra also show a low intensity (around 5%) magnetic sextet, S3, with parameters typical of hematite [45,46].

As mentioned above, however, the spectrum recorded from the sample 4H located close to heater contact is quite different. Although the nature of the central paramagnetic region appears to be the same than in the rest of the samples, it contains a much more intense and defined magnetic component characterized by larger hyperfine magnetic fields. This component was fitted to two different sextets, S3 and S4. Sextet S3 is typical of hematite and S4 probably corresponds to a defective hematite phase ("hematite-like phase") [47]. This sample still contains a noticeable goethite concentration. It is well-known that the dehydration of goethite may result in the formation of hematite [48,49]. Therefore, it seems plausible that this sample, which has been collected close to the heater, contains hematite as consequence of the loss of OH groups in goethite brought about by the local heating. In addition, these species, or at least a fraction of them, may result from a high temperature corrosion process occurring at the C-steel heater surface. This sample also contains Fe^{2+}. In fact, is in this sample where it can be observed more clearly due to the lower concentration of goethite whose spectrum overlaps strongly with the Fe^{2+} doublet. The result indicates that heating does not affect the Fe^{2+} species probably because it is comfortably sited within the clay mineral structure and results difficult to oxidize or to a slightly increase of Fe^{2+} within the smectite structure. The presence of magnetite is discarded in all samples analysed.

Table 7. Hyperfine parameters obtained from the fit of the spectra presented in Figure 12

Hyperfine parameter	D1	D2	D3	S1	S2	S3	S4
δ (mms^{-1})	0.36	0.38	1.03	0.37	0.33	0.35	0.37
Δ/2ε (mms^{-1})	0.44	0.81	2.41	-0.15	-0.14	-0.20	-0.20
H (T)	--	--	--	27.4	20.1	51.0	47.6

δ, isomer shift; Δ, quadrupole splitting, aplies to doublets; 2ε, quadrupole shift, apllies to sextets; H, hyperfine magnetic field.

Table 8. Relative areas obtained from the fit of the spectra presented in Figure 12

Area (%)	Distance to heater (cm)	D1 $Fe^{3+}O_h$	D2 $Fe^{3+}O_h$	D3 Fe^{2+}	S1 α-FeOOH	S2 *α-FeOOH*	S3 α-Fe_2O_3	S4 *α-Fe_2O_3 like*
Reference	--	41	29	3	16	7	5	--
6G	8.33	37	24	2	25	7	5	--
5M	5.00	37	21	3	29	5	5	--
4H	1.67	30	23	4	20	--	12	21

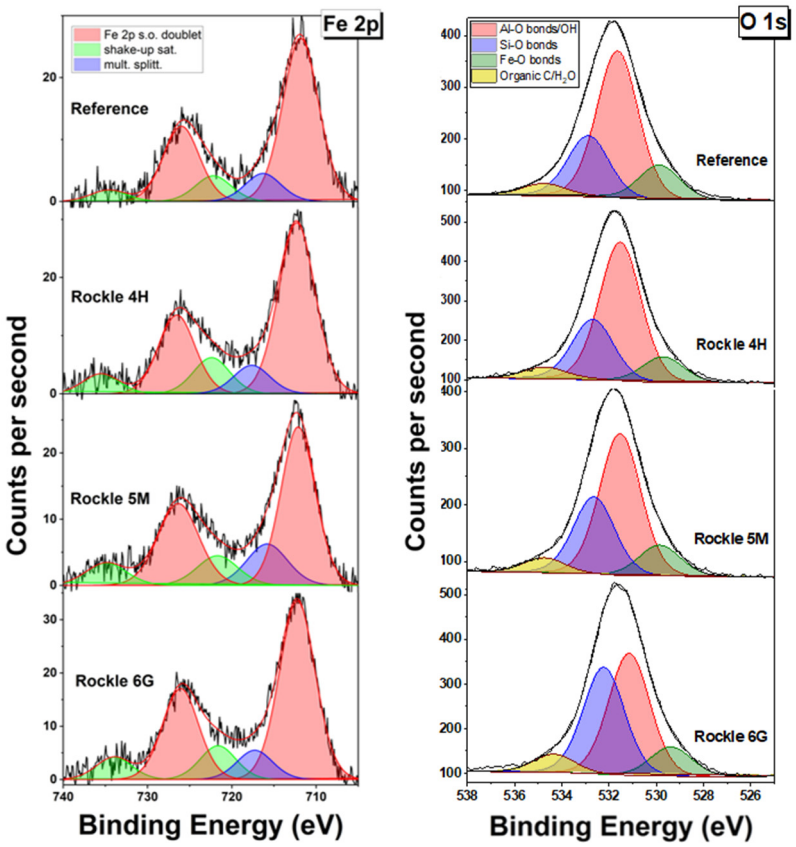

Figure 10. XPS narrow scan Fe 2p and O 1s spectra recorded from the Rokle samples: reference, 4H: close to heater interface, 5M: middle, and 6G: close to granite interface; i.e. at 1.67 cm, 5.00 cm and 8.33 cm from heater contact, respectively.

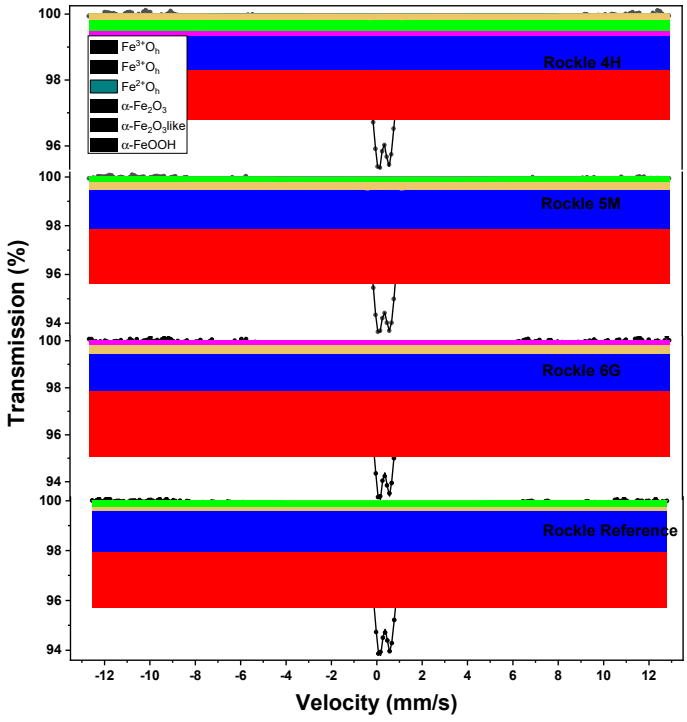

Figure 11. Room temperature ^{57}Fe Mössbauer spectra recorded from the Rokle samples: reference, 4H: close to heater interface, 5M: middle, and 6G: close to granite interface; i.e. at 1.67 cm, 5.00 cm and 8.33 cm from heater contact, respectively.

3.3. Geochemistry

The geochemical analysis of the samples consisted on chemical analyses of the main elements in the total fraction of the bentonite material by: a) XRF, b) total carbon and sulfur content by combustion, and c) Fe speciation (Fe(II)/Fe(III)) analysed via NH_4HF_2-H_2SO_4 leaching tests.

The main changes observed in all the samples are related with iron content, which increased between in all samples with respect their reference values (Figure 12 and Table S3-S4 from Supplementary Material), although other variations are observed. In all the Ca/Mg-bentonites (Febex and Ibeco), the calcium content slightly decreased increasing sodium, potassium and strontium contents. However, in all the Na-bentonites (Asha 505 and MX-80), sodium content decreased increasing calcium, potassium and strontium content. This seems to indicate a tendency to equilibrate the composition at interlayer sites in all type of bentonites, prevailing bivalent cations (see Section 3.4). In addition, those bentonites which an initial higher iron content (Asha 505, Rokle and MX-80) are able to acquire more amount of iron in their structure than those having an initial lower iron content (Figure 12). On the other hand, although the amount of Fe(II) is low with respect to total Fe, Fe(II) content increased at the heater contact (Figure 13, Table S5 from Supplementary Material). Mg content is the cation that less change in comparison to sodium and calcium, but there is a tendency to increase in the samples with a higher initial Fe content.

Regarding to carbon and sulfur contents (Table 9), no significant differences are observed, except the presence of organic matter in the MX-80 bentonite block 1, but values being lower than in the reference value.

3.4. Physico-chemical properties

The main physico-chemical properties analysed were external (BET) and total surface (SA) areas, total cation exchange capacity (CEC), cation exchange population and the distribution of soluble ions in aqueous extracts.

Total surface area is an important parameter related to the water absorption and swelling capacity of bentonites. It determines the amount of water needed for hydrating all the clay particles. The lower the particle size, the higher total surface area. The external surface area of the stacks of layers, determined by N_2-BET measurements, corresponds to both the external faces and the edges of the montmorillonite particles since in the adsorption of non-polar molecules, such as N_2, the layered structure remains closed. External BET and total surface area values are given in Table 9. No significant changes are observed in total SA, but a decrease of the external BET surface area is observed in all the retrieved samples, being more stressed at the heater contact (Figure S5 and Table S6 from the Supplementary Material).

The N_2 adsorption-desorption curves of reference and retrieved samples are shown in Figure S6 from Supplementary Material. The isotherms are Type IV indicating adsorption on mesoporous material (IUPAC classification). When the relative pressure (P/P_0) is higher than 0.4, a hysteresis loop appeared, indicating that capillary condensation occurs in mesopore and macropore; adsorption being dominated by capillary condensation and evaporation. At $P/P_0 < 0.4$, the adsorption and desorption isotherms coincide with each other, and the adsorption is dominated by van der Waals force at this stage. The N_2 adsorption-desorption curves differ from all the reference values and are significantly affected by heating. Regarding the type of hysteresis loops, they can reflect pore morphology in porous material. The hysteresis loop for all the samples, except for the MX-80 bentonite, is between H2 and H3 type, indicating the coexistence of ink bottle-like pores and many slit pores formed by the plate-shaped minerals [50]. For MX-80 the hysteresis loop is close to H4 type, indicating the existence of slit-like pore produced by similar layered minerals. According to the modification of the hysteresis loop, all retrieved samples seems to increase the of ink bottle-like pores.

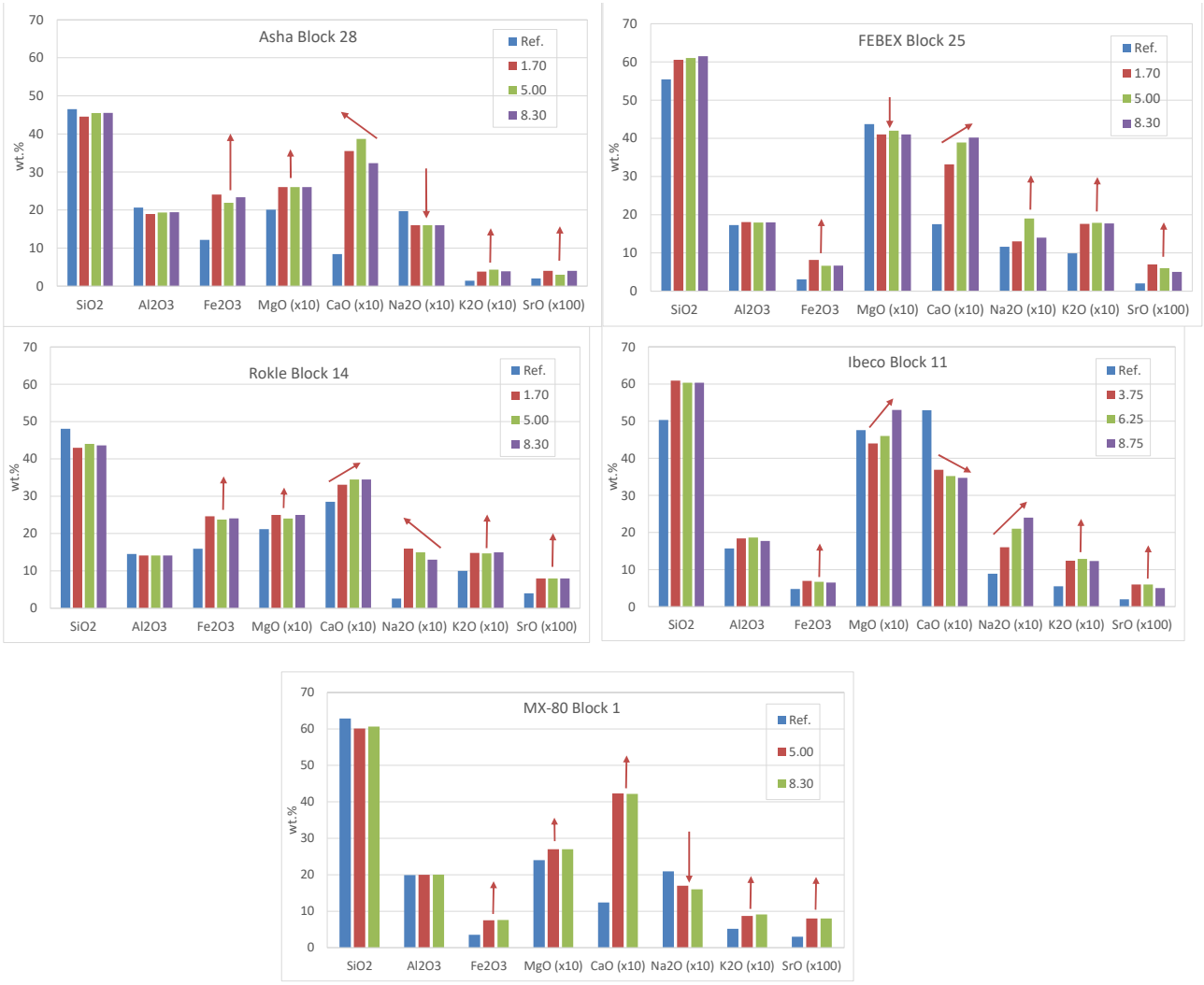

Figure 12. Chemical composition of the solid phase (total fraction) prior and after dismantling of the ABM5 Experiment as a function of the heater distance (1.70 (H), 5.00 (M) and 8.30 (G) cm).

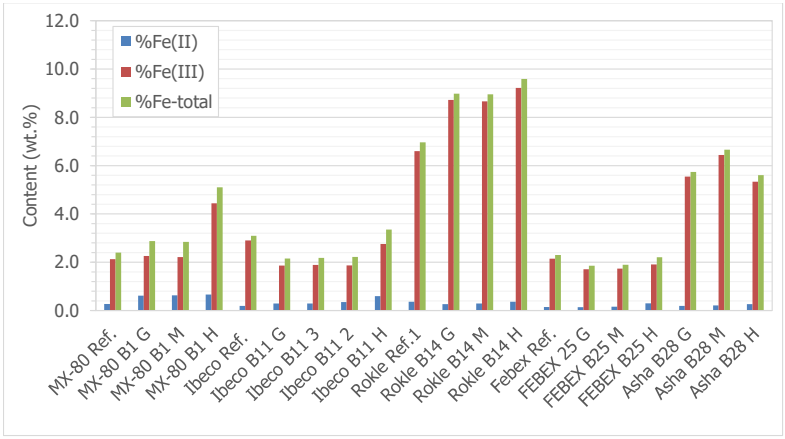

Figure 13. Iron content in the solid samples prior and after dismantling of the ABM5 Experiment: Fe(II), Fe(III) and Total Fe.

Table 9. Total Carbon, Total sulfur, Total surface area (SA) and BET surface area obtained after dismantling of ABM5.

Sample	Distance to heater (cm)	Water content (%)[1]	C_{Total} (wt.%)	$C_{Inorg.}$ (wt.%)	$C_{Org.}$ (wt.%)	S_{Total} (wt.%)	Total SA (m^2/g)	S_{BET} (m^2/g)	CEC (meq/100g)
Asha 505 Ref.[2]	--	13.1	0.03	0.02	0.01	0.02	--	--	88.6
Asha B28 G	8.3	16.8	0.10	< 0.1	< 0.1	< 0.1	585	65.41	85.8
Asha B28 M	5.0	17.6	0.16	< 0.1	< 0.1	< 0.1	574	55.99	83.9
Asha B28 H	1.7	13.4	0.19	< 0.1	< 0.1	< 0.1	584	61.49	81.3
FEBEX Ref.	--	14.3	0.12	0.08	0.04	<0.05	628 ± 4	59.2 ± 5	98.1
Febex B25 G	8.3	13.8	0.08	< 0.1	< 0.1	< 0.1	640	38.01	97.6
Febex B25 M	5.0	13.3	0.09	< 0.1	< 0.1	< 0.1	627	45.76	96.5
Febex B25 H	1.7	13.2	0.05	< 0.1	< 0.1	< 0.1	622	36.20	93.1
Rokle Ref.	--	17.2	0.27	0.10	0.17	0.02	573 ± 5	82.8 ± 0.3	73.8
Rokle B14 G	8.3	8.6	0.26	< 0.1	< 0.1	< 0.1	538	66.90	73.1
Rokle B14 M	5.0	8.9	0.22	< 0.1	< 0.1	< 0.1	549	64.09	73.0
Rokle B14 H	1.7	8.1	0.21	< 0.1	< 0.1	< 0.1	517	58.70	70.3
Ibeco Ref.	--	14.7	0.79	0.62	0.17	0.23	611 ± 2	57.4 ± 0.4	90.2
Ibeco B11 G	8.75	13.1	0.13	< 0.1	< 0.1	< 0.1	706	49.75	97.1
Ibeco B11 3	6.25	13.1	0.13	< 0.1	< 0.1	< 0.1	688	48.98	97.9
Ibeco B11 2	3.75	13.6	0.15	< 0.1	< 0.1	< 0.1	660	45.04	88.6
Ibeco B11 H	1.25	13.6	0.10	< 0.1	< 0.1	< 0.1	680	51.71	95.0
MX-80 Ref.	--	10.6	0.28	0.08	0.20	0.24	481 ± 1	29.7 ± 0.2	83.6
MX 80 B1 G	8.3	11.6	0.27	0.16	0.11	0.16	523	21.72	84.1
MX 80 B1 M	5.0	11.6	0.29	0.22	0.07	0.22	542	18.91	87.6
MX 80 B1 H	1.7	11.4	0.24	0.22	0.02	0.22	528	22.48	87.8

[1]air dried; [2] [1]; G: granite contact; H: Heater contact

CEC is one of the most important parameters for characterising the bentonite adsorption behaviour is the cation exchange capacity (CEC). This parameter is equivalent to the total negative surface charge of a clay mineral and reflects the degree of reactivity of the bentonite because CEC is related to the capacity of adsorption and retention of ions and to the swelling capacity of the bentonites. This parameter is liked with the interlayer cations, who nature is also an important issue because the cation composition at exchange sites affects not only the exchange properties but also the plasticity, the swelling capacity and the rheological behaviour. Values of CEC and cation exchange population are observed in Figure 14 and Table S7 from Supplementary Material. Slight but not significant variations are observed in CEC values with respect to initial values, slightly decreasing towards heating source, except for MX-80 bentonite block located at the bottom part. However, there is a complete readjustment in the cation exchange composition in all bentonites. Na-bentonites (Asha 505 and MX-80) reduce its sodium content increasing calcium. In the case of Mg-Ca bentonites (Rokle, Ibeco, FEBEX), sodium content increased, as well as the calcium content, being the higher sodium increase the lower the initial sodium content at exchange sites in the bentonite (e.g., see Rokle with respect to FEBEX bentonite). Magnesium content tends to decrease in all samples, except in MX-80 bentonite, where values increase at heater contact. It should be taken into account that cation exchange concentration was corrected with respect to soluble salts from pore water, which may affect mainly to calcium content.

Aqueous extracts were performed for obtaining ion inventories and ion distributions along the bentonite blocks (Table S8 and Table S9 from Supplementary Material). It should be taken into account that only Cl^-, F^-, and Br^- can be considered as conservative ions during the leaching tests, whereas the rest of anions and cations are controlled by mineral dissolution/precipitation processes and ion exchange reactions. Therefore, extractions conditions were selected to suppress mineral oxidation, by working in an oxygen-free atmosphere, and to avoid large modifications of cation concentration at exchange sites by carbonates dissolution, which affect the cation distribution in the aqueous

extract solution. The time needed to attain carbonates equilibrium in bentonites usually requires more than six days, affecting greatly the exchange composition (e.g., [12, 51]. Therefore, all the tests were performed for one day.

The soluble salts obtained from the samples taken after ABM5 experiment are shown in Figure 15. pH in the aqueous extracts is neutral with values between 7.6 and 7.8. Chloride values increased in all samples with respect to the initial reference values but the content is lower at the heater contact (H) than at granite contact (G), indicating a diffusion process through the compacted bentonite. It is interesting to see also the increased values of fluoride and bromide contents coming from the infiltrating Äspö groundwater (Table 2). Sulfate content depends on the type of bentonite and its initial pore composition, although values increase towards heater contact in most samples (Figure 19). Alkalinity values ranges between 0.3 and 0.7 mmol/100 g expressed as HCO_3^-. Therefore, dissolution/precipitation processes of carbonates control the pH of the bentonites pore water and cation exchange reactions. This is observed by cation content variations (Figure 16), which increased in all samples with respect to reference samples although with a tendency to decrease as a function of heater contact, except for the Na-bentonites. Mg also increased at heater contact in the Na-bentonites (Figure 16).

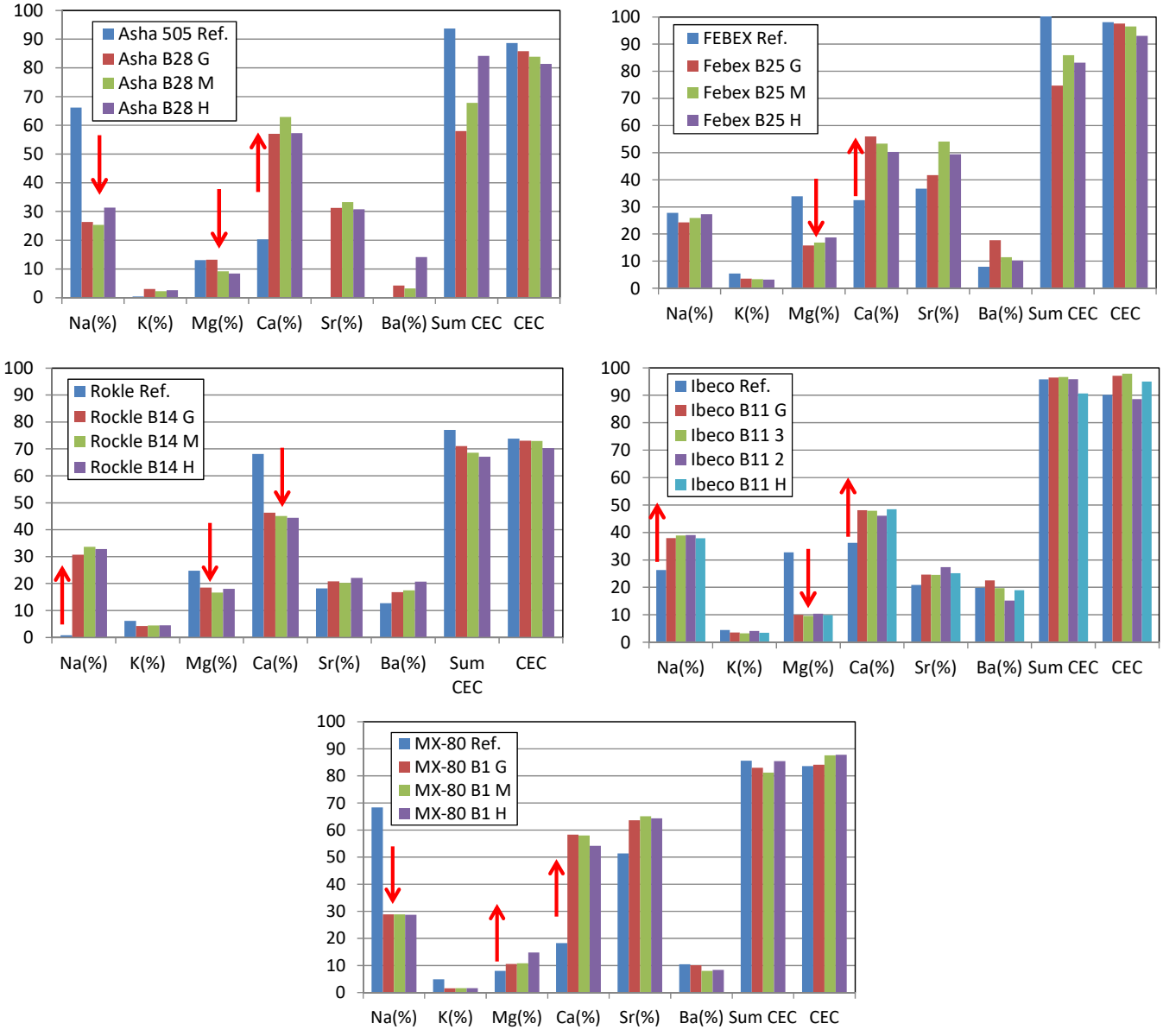

Figure 14. Cation exchange population after dismantling of the ABM5 experiment. Sr and Ba percentage is multiplied by 100 and 1000, respectively.

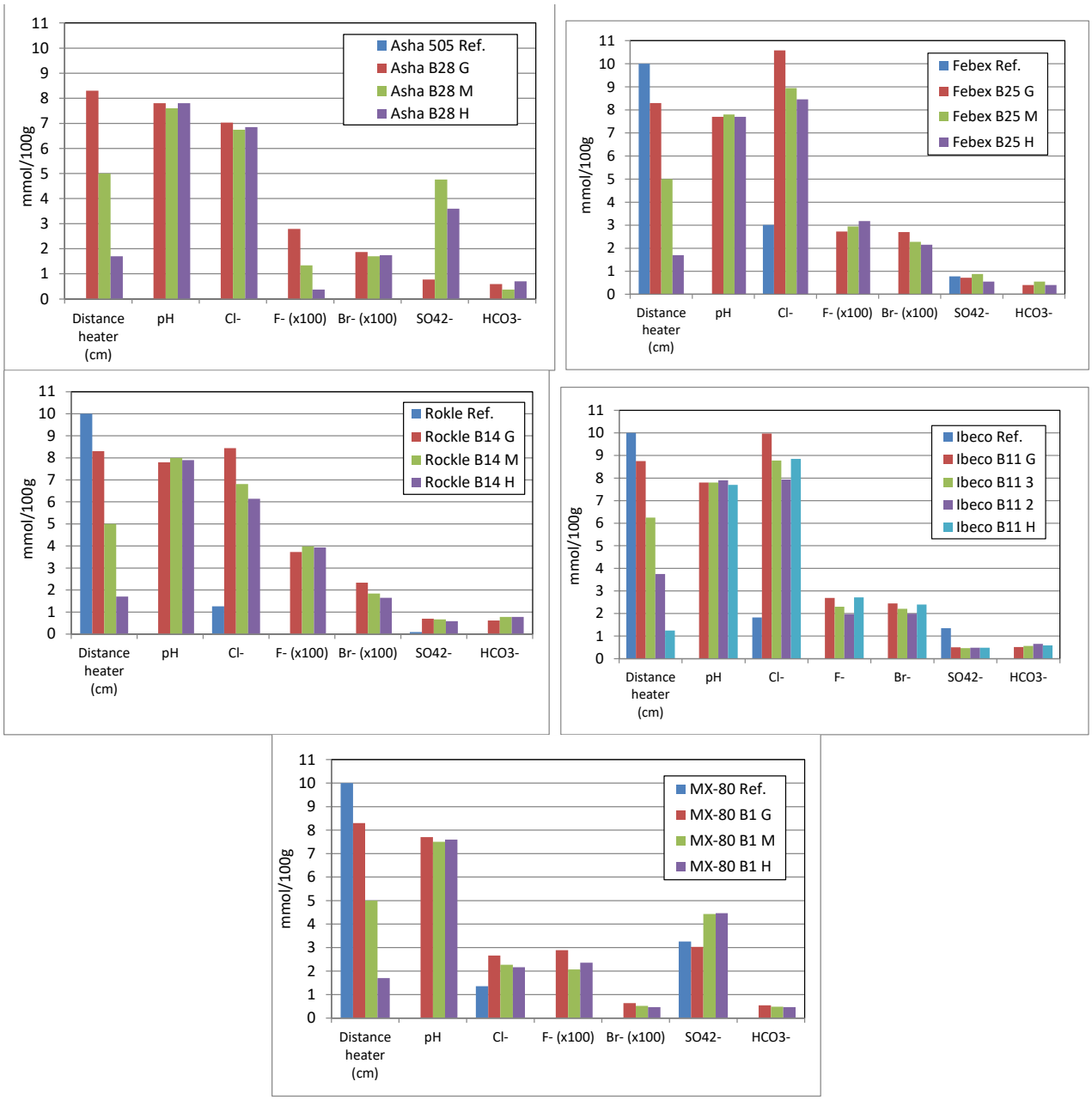

Figure 15. Anion distribution as a function of the heating contact obtained from leaching tests (in mmol/100g). Reference data for chloride and sulfate are given for comparison.

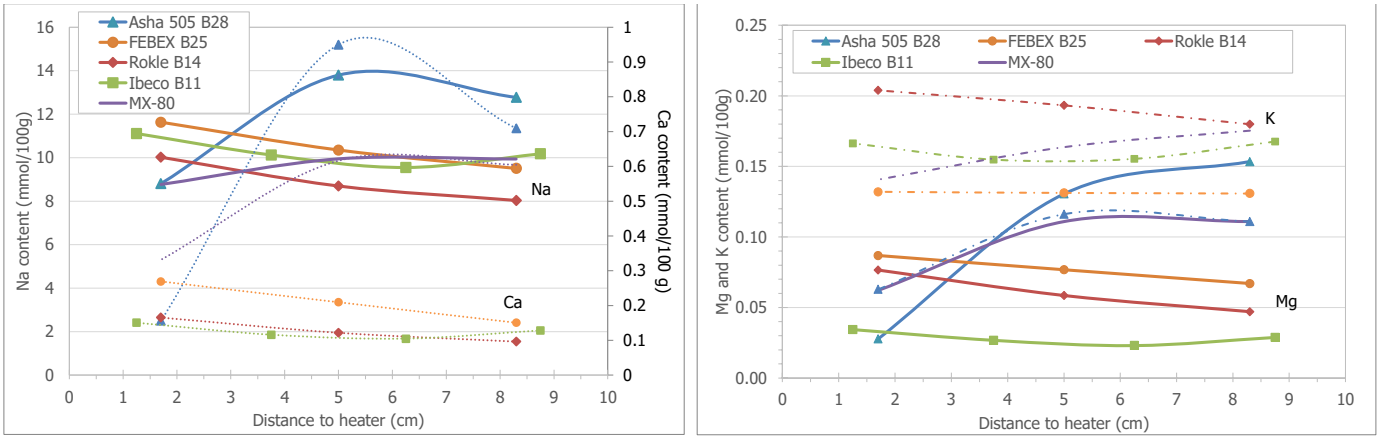

Figure 16. Cation distribution as a function of the heating contact obtained from leaching tests (in mmol/100g). Reference data for chloride and sulfate are given for comparison.

3.3. Pore water chemistry

Pore water chemistry was obtained by squeezing at a pressure ranging between 20 and 30 MPa (Table 10), depending on the water content and dry density of the samples. The more water content of the sample, the lower squeezing pressure was needed (otherwise for dry density). The squeezing tests were performed with the pre-requirement of obtaining some amount of water enough for chemical analysis at the lowest squeezing pressure. This is because the greater the squeezing pressure, the greater the ease with which water bound to clay particle surfaces is expelled [25]. A representative pore water sample of homogeneously distributed electrolytes in the bulk aqueous phase requires avoiding the sampling of different portions of the diffuse layer water. Because of the high water content of the samples, pore water could be extracted at low squeezing pressures in a few days (3-7 days). It is worthy to note that the hole piece of a bentonite block was used for squeezing tests, so the pore water chemical composition represents an average value from each bentonite block from the granite contact to the heater contact, in spite of there is a small solute gradient between these interfaces as shown in Figure 15 and 16.

pH of the pore waters is neutral/slightly alkaline, with values ranging between 7.1 to 7.9 (Table 11). The salinity of the pore water is very high due to both the infiltrating marine Äspö groundwater (chloride content of 8580 mg/L (241.9 mmol/L, Table 2), and the high salinity of the initial bentonites pore water (Table S11 from Supplementary Material). After dismantling, ionic strength pore waters ranges from 0.26 to 0.91 M, the lower values being at the bottom part of the bentonite column (MX-80 bentonite block 1).

Table 10. Characteristics of the squeezing tests performed from bentonites after ABM5 dismantling.

Core Sample	Initial mass (g)	Initial dry density (g/cm^3)	Initial w.c. (%)	Time elapsed (days)	Squeezing Pressure (MPa)	Pore fluid extracted/ mass loss (g)	Final mass (g)	Final dry density (g/cm^3)	Final w.c. (%)	Efficiency (%)[(1)]	Efficiency (%)[(2)]
Asha B28	208.74	1.53	28.6	7	20	7.3	201.44	1.62	26.4	45.3	15.7
FEBEX B25	369.23	1.49	26.6	7	30	10.1	359.15	1.62	24.8	58.8	13.0
Rokle B14	292.90	1.60	31.2	5	20	10.8	282.06	1.67	25.4	23.3	15.6
IBECO B11	187.07	1.49	36.0	3	20	7.1	180.00	1.55	28.7	49.5	14.3
MX-80 B1	201.08	1.51	35.8	3	30	5.8	195.26	1.60	25.9	17.2	11.0

[(1)] Efficiency (%) = (Collected water x 100)/Extracted water; [(2)] Total Efficiency (%) = (100 x extracted water)/($P_{initial} - P_{dry}$)

The chemical composition of all bentonite pore waters is dominated by Cl^-, Na and Ca, except for the more dilute pore water from MX-80 block 1, which is Na-Cl water type. The Äspö granitic groundwater (Ca-Na-Cl water type) is very saline with an ionic strength of 0.91 M (Table 2). During infiltration, the bentonite pore waters changes from mainly initial Na-Cl or Na-SO_4 water type (see Table S11 from Supplementary Material), towards a Na-Ca-Cl pore water in all bentonite blocks analysed, except for MX-80 block 1, which changes from Na-SO_4 to Na-Cl water-type.

Chloride concentration increased in all samples, values ranging between 25000 mg/L (705.2 mmol/L) to 5800 mg/L (163.6 mmol/L), from the top to the bottom of the bentonite package, the lower values being located at the bottom part (MX-80 block 1). It should be taken into account that the initial chloride contents of 6600, 2800 and 1100 mg/L for reference FEBEX, IBECO and MX-80 bentonites, respectively (Table S11 from Supplementary Material). The same behaviour occurs for Na and Ca, showing increased values.

Mg concentration in the pore water increased in all samples after the experiment, but variations depend on the initial composition of the bentonite pore water, being higher for the FEBEX bentonite [12,52] (Table S11). Sulfate contents are similar in all the bentonites, with concentrations ranging between 1100 and 1800 mg/L, the higher values corresponding to Ibeco block 11 and MX-80 block 1 bentonites, which have higher initial reference values (4300 and 9300 mg/L, respectively, Table S11).

Alkalinity values are low, similar to that of the groundwater, values ranging from 0.76 to 1.18 meq/L, the highest value belonging to the MX-80 Block 1 pore water. However, these values seem to be much lower than those detected in reference samples (Table

S11). It´s interesting to note the presence of TOC, acetate, and formate in the pore waters (Table 11).

The geochemical code PHREEQC, version 3.4 [53] and the Thermoddem database [54] were used for equilibrium modelling and saturation indices calculations (Table S10 from Supplementary Material) at 25°C. The saturation indices indicate that the pore waters from all samples are saturated with respect to calcite, gypsum, celestine, barite, calcite, dolomite, magnesite, barite and quartz (except Rokle); and undersaturated with respect to halite.

Table 11. Chemical composition of the pore water extracted from the AMB5 bentonite blocks.

Sample	Asha Block 28 S	FEBEX Block 25 W	Rokle Block 14 NW	IBECO Block 11 S	MX-80 Block 1 IN
Sq. Pressure (MPa)	20	30	20	20	30
Water content (%)	28.6	26.6	31.2	36.0	35.8
Total weight (g)	208.74	369.23	292.90	187.07	201.08
Water type	Na-Ca-Cl	Na-Ca-Cl	Na-Ca-Cl	Na-Ca-Cl	Na-Cl
pH	7.9	7.3	7.7	7.1	7.5
Alkalinity (meq/L)	0.94	0.90	0.90	0.76	1.18
F^- (mg/L)	< 1	< 1	< 1	< 1	< 1
Br^- (mg/L)	152	195	128	112	28
Cl^- (mg/L)	25000	24000	24000	19000	5800
SO_4^{2-} (mg/L)	1100	1100	1100	1700	1800
NO_3^- (mg/L)	6.1	< 1	< 1	3.3	1.3
Si (mg/L)	210	7.0	3.6	200	8.5
Al (mg/L)	< 0.3	< 0.3	0.08	< 0.3	0.09
Na (mg/L)	9620	8100	9460	8040	3410
K (mg/L)	185	110	150	256	59
Ca (mg/L)	6100	4450	4350	3175	575
Mg (mg/L)	450	1500	560	850	180
Sr (mg/L)	49	60	47	30	12
Ba (mg/L)	0.45	0.52	0.55	< 0.3	0.33
Fe (mg/L)	< 0.3	1.4	< 0.03	< 0.3	0.04
Cu (mg/L)	0.67	0.70	0.39	1.0	0.19
B (mg/L)	4.5	0.90	0.26	3.1	0.07
Mn (mg/L)	1.3	2.8	0.52	8.9	0.59
Mo (mg/L)	< 0.3	< 0.3	0.37	< 0.3	0.67
Ni (mg/L)	< 0.3	1.7	0.14	3.9	2.0
Ti (mg/L)	< 0.3	< 0.3	< 0.03	< 0.3	< 0.03
V (mg/L)	< 0.3	< 0.3	< 0.03	< 0.3	< 0.03
Zn (mg/L)	0.41	< 0.3	0.06	0.51	0.23
$S_2O_3^{2-}$ (mg/L)	< 1	< 1	< 1	< 1	< 1
Acetate (mg/L)	51	< 1	48	21	1.8
Formate (mg/L)	35	< 1	2.0	741	14
TOC (mg/L)	n.d.	57.1	97.1	n.d	44.2

4. Discussion

From the geochemical point of view, specific long-term requirements for the function of a bentonite to isolate the canisters from water and retard the migration of radionuclides is to maintain a suitable chemical environment for the canister integrity and radionuclide retention over time, buffering possible alteration/deterioration processes of the bentonite. In this section a discussion of results about the possible modifications of the bentonites reacting due to changes in the initial conditions and different types of perturbations after 4.4 years of experiment is given.

4.1. Physical properties variations

It is interesting to note the increase of porosity, from 29-39% to 45-48% of the compacted bentonite blocks after the infiltration of the saline groundwater (see microstructure of clay minerals Fig. 9). After 4.4 years of artificial hydration and heating, samples increased their water content up to ~30 ± 2%, and the dry density decreased up to ~1.52 ± 0.05 g/cm^3 due to bentonite swelling capacity. Two factors have probably influenced the mineralogical/geochemical behaviour in this experiment and the physico-chemical properties of the bentonites. First, due to the bentonite/groundwater infiltration and final salinity of the pore water the relationship between external (pore water) and internal (interlayer water) must have been readjusted during the experiment due to the decrease of thickness of the double diffuse layer (DDL), increasing the amount of available water (free water layer) for geochemical reactions. Second, experiment was performed at constant temperature of 50°C during most of the experimental time (3.45 years). Temperature was increased to 150°C for a period of 6 months and to 250°C for the final 6 months (Figure 2). These final overheating periods probably provoked an impact on water distribution and final density, as observed after dismantling [3]. Dry density tends to increase towards heating contact and water content is higher at the bottom part of the bentonite package, in spite of supposed complete saturation of the bentonites. Indeed, degree of saturation varies from 93 to 100% from the top to the bottom of the bentonite package probably due to steam-bentonite interactions which affected to the bentonites/groundwater interactions. No steady state geochemical conditions are observed after dismantling, some modifications being more stressed in bentonite blocks located at the top (Asha 5050, FEBEX and Rokle) than at the bottom part of the bentonite package (IBECO and MX-80). For example, calcite content in IBECO bentonite samples (Block 11) was drastically decreased, whereas calcite precipitation is observed in the rest of upper and below bentonite blocks. The variation in CEC values is not the same in samples located at the bottom part (IBECO block 11 and MX-80 Block 1) with respect to those located at the top part.

4.2. Mineralogical and geochemical alterations

The high thermal conditions of this experiment (up to 250°C) could has altered the bentonite clay minerals to non-swelling minerals affecting the performance of the barrier. However, transformation of montmorillonite to illite is discarded, probably to low variations in the potassium content both in pore waters and exchange sites, even though the high temperatures. No modifications are observed in the clay mineral fraction after ethylene glycol treatment of the samples analysed (Figure 6).

In addition, metallic iron produced by corrosion of the heater could lead to [29]: a) reduction of Fe(III) to Fe(II) in clay mineral structure, affecting the layer charge, b) dissolution/alteration of montmorillonite to other minerals, and c) cementation processes affecting plasticity, sweeling or hydraulic conductivity of the bentonites. Trioctahedral smectites were found in previous experiments, such as ABM1, ABM 2 experiments [30, 55], FEBEX *in situ* test [51], TBT experiment [55], and Prototype experiment [56]. However, in this work, no Mg- or Fe-rich trioctahedral smectites were detected despite the decrease of Mg at exchange sites and the increase of iron due to the corrosion of the C-steel heater. This is in agreement with other ABM5 studies [3,4].

The most interesting modifications found in the samples close to heater contact were the increase of gypsum, calcite and presence of siderite and monohydrocalcite, pyrite and Na-clinoptilolite. However, not all these mineral phases were found in all bentonites (Figure 5 and Table S1 from Supplementary Material). Goethite and hematite (due to heat), as the main Fe-oxides, and siderite were the corrosion products detected. Magnetite was not found (even by Mössbauer spectroscopy analysis) in spite of the increase of Fe(II) at the heater contact. Siderite neoformation was also observed in other ABM5 studies [3]. Hematite was not observed in all samples, only in Asha 505 Block 18, Rokle Block 14 and MX-80 Block 1. These bentonites contained higher amounts of goethite (Asha 505, Rokle) or siderite/pyrite (MX-80) in reference samples, and precipitation of hematite may be due to heating (goethite to hematite transformation by heat), or to siderite dissolution/pyrite oxidation in the case of MX-80. However, pyrite and siderite are still observed in all retrieved MX-80 samples analysed. Therefore, the presence of goethite or hematite may be due to heater corrosion process under different oxic/anoxic environmental conditions, being favoured neoformation of goethite in presence of oxygen.

Dissolution/precipitation processes of calcite are observed, which seems to be affected by temperature and water vapour fluxes. It is interesting to note the dissolution of calcite in IBECO bentonite Block 11, which is not observed in the rest of bentonite blocks located at the top and the bottom of the bentonite package, where an increase of carbonates is indicated. Monohydrocalcite is a neoformed at heater contact in Asha 505 bentonite. Gypsum content decreased in MX-80 bentonite Block 1 at heater contact but increased in Asha 505 Block 28 and saturation indices from pore waters are oversaturated with respect to gypsum and anhydrite. However, anhydrite has not been found.

An increase of free silica can be ruled out, although an increase of tetrahedral charge in some clay minerals particles is observed. No significant variations in cristobalite/trydimite and feldspars mineral phases were found, although the intensity of their reflections increased in some samples.

4.3. Redistribution *of CEC and exchangeable cations*

The cation composition at exchange sites for the different bentonites have been modified after 4.4 years. Changes in exchangeable cation composition can be explained on the basis of equilibration with Äspo saline (I=0.91 M) groundwater (Table 2), which is enriched with Ca and Na salts, more than due to chemical interaction between the buffer blocks with each other and to temperature. The variation of the type of exchangeable cations in all bentonites seems to indicate that concentration tends to equilibrium with groundwater and to be homogeneous in the whole bentonite column, prevailing bivalent cations at exchange sites. However, complete equilibration of the cation occupancy has not been achieved after 4.4 years of experiment. Those calcium bentonites increased their sodium content, and those sodium bentonites increased their calcium content, exchangeable magnesium being replaced and decreased in all the samples, except in MX-80 block 1 located at the bottom of the column. In spite of available and increased magnesium content in the pore water, no other additional magnesium-bearing mineral phases were detected in the bentonites by SEM, XRD or FTIR (Table S1).

These cation exchange variations may involve the decrease of the external surface area values observed in all samples. This decrease may be explained by two mechanisms: a) Missana et al. [57] analysed the size of clay colloids as a function of the exchangeable cation and layer charge location, showing that the presence of above 80% divalent cations at exchange sites favours the formation of large particles, but also that an increase in tetrahedral charge produces an increase in clay colloid size, independently of the main interlayer cation. An increase of the particle size implies a decrease of the external surface area; b) colloid properties (size and mobility) of the clay minerals are also affected by an increase of the electrolyte concentration due to aggregation of clay particles. Because the increases of the pore water salinity, divalent cations and the tetrahedral charge observed, an increase of the size of clay particles is expected, favouring the decrease of the external surface area.

The CEC values seems to slightly decrease towards the heater contact from the upper part of the bentonite column towards the middle part (Asha 505 Block 28, FEBEX Block 25 and Rokle Block 14), with variations of -7.3, 5.0 and -3.5 meq/100 g in samples at heater contact with respect to reference values. However, this decrease is not observed in the two blocks located at the bottom part of the column (IBECO block 11 and MX-80 Block 1), where changes are in positive, increasing about 4.5 meq/100 g.

The decrease of CEC at heater contact has been observed in other *in situ* experiments [4, 51, 58-61]. The decrease on CEC values may be related to high-temperature conditions, water vapor formation [62], a lower content of smectite or to a modification of the crystal structure of the smectite clay particles, decreasing the layer charge. The variation in smectite and total phyllosilicates content in most of the samples seem to maintain in values similar to reference values, within the experimental error. Thus, other explanations need to be given. Interestingly, sum of exchangeable cations is similar to total CEC value, except in the upper bentonite blocks (Asha 505 Block 28, FEBEX Block 25), where a decrease of exchangeable Mg was detected as expense of an increase of exchangeable Ca. This observation was observed twice after repeating the determination, and also detected by [4]. The increase of calcium at exchange sites may be indicative of an increased calcite content in the retrieved samples, as observed in XRF data (Table S3 and Table S4) and in [3], which could lead to its dissolution during extraction. However, this shouldn´t affect to magnesium content at exchange sites. This decrease is not well understood.

A decrease in the CEC may be caused in this experiment by: a) the collapse of clay particles, particularly of highly charges smectites [63], b) the collapse of clay particles caused by large ionic strength, which generally reduce the swelling pressure (e.g. [64,65]), c) extensive drying process due to increased Ca/Mg fixation and/or K fixation at interlayer sites [66]. As shown by the results all these factors: increase of layer charge, increase of tetrahedral charge (Table 5), high salinity and drying are involved in this system. However, the differences observed from top to bottom of the bentonite column seems to indicate that the temperature and water vapor fluxes have affected to the CEC parameter.

4.4. Pore water chemistry variations

Intrinsic properties of bentonites, such as CEC, presence of soluble minerals (e.g., calcite, gypsum, ..) and low hydraulic conductivity and permeability of compacted material (i.e., solute transport by diffusion) imply a large buffering capacity for many geochemical processes. The chemical state of the buffer is defined by the bentonite composition (clay minerals and accessory minerals) and the pore water composition. Consequently, the chemical stability of the bentonite, this is the alkalinity and redox buffering capacity, will be firstly controlled by the bentonite-water interactions and the resulting pore water chemistry (pH, redox potential, ionic strength, ionic composition, speciation and complexation). In addition, the knowledge of the porewater chemistry in the clay barrier is essential for performance assessment purposes in a nuclear waste repository, since the porewater composition controls the processes involved in the release and transport of the radionuclides.

In most studies performed with bentonites is observed that the bentonite composition controls the pore water chemistry evolution after their interaction with an infiltrating groundwater, and it is basically controlled by ion exchange reactions and dissolution/precipitation of the more soluble trace minerals of the bentonite [67-69]. However, this depends on the salinity of the infiltrating water, as observed in this experiment. In the case of a saline Äspö groundwater/bentonite interaction, the pore water chemistry depends on the advection-diffusion rate of the infiltrating groundwater (which depends on the bentonite dry density and water content, i.e., porosity), and it is basically controlled by ion exchange reactions.

The initial bentonite pore water was modified in all bentonite blocks after their interaction with the saline Na-Ca-Cl groundwater. However, the pore water composition is not at equilibrium in each bentonite block and in the whole bentonite package since an advective-diffusion infiltration process of the conservative ions (Cl^-, Br^-, F^-) is still ob-

served towards the heater after 4.4 years of experiment. A clear evolution of the pore water is observed after groundwater infiltration. The bentonite pore waters changes from mainly initial Na-Cl or Na-SO_4 water type (see Table S11 from Supplementary Material), towards a Na-Ca-Cl pore water in all bentonite blocks analysed, except for MX-80 block 1, which changes from Na-SO_4 to Na-Cl water-type. The final ionic strength values of the pore waters (0.82-0.91 M) are similar in the upper bentonite blocks (Asha 505, FEBEX, Rokle) but lower at the bottom part of the package (IBECO and MX-80), with values of 0.69 and 0.26 M, respectively. Probably water-vapor fluxes increased the salinity of the pore waters at the top part. However, variations in cation composition of the pore water indicate that pore water is controlled by equilibration of infiltrating water with main accessory minerals and the exchanger (cation exchange sites and surface complexation sites). In any case, pore water chemistry data (Table 11) and anion inventory (Figure 15) indicate that saturated bentonites (including cation occupancy and pore water composition) are not in equilibrium with the external infiltrating ground water.

pH values are neutral in all pore water samples analysed indicating the buffering capacity of the bentonite via protonation/deprotonation reactions and dissolution/precipitation of mainly calcite. Alkalinity values decreased in all samples and saturation indices from pore waters indicate saturated conditions with respect to calcite.

Organic matter (TOC) and volatile fatty acids (VFAs), such as acetate and formate were found in pore water samples from the different bentonites (Table 11). At this interface, factors of temperature and possible hydrogen, available due to corrosion processes, may reflect the reduction CO_2 to produce acetate and then formate. On the other hand, acetate and formate are also produced as fermentation products through the degradation of organic matter under anaerobic conditions. However, the implication of microorganisms in different reactions at the heater interface could not be confirmed. More interesting is the idea that oxic corrosion and hydrolysis of carbon-containing steels (liner, Heater#2, etc.), leading to the generation of H_2, CO_2 and hydrocarbons (alkanes, alkenes and carboxylic acids), is the possible main process for the presence of acetate and formate in the pore water close to the heater interface [51]. However, no evidence of completely anoxic redox conditions and hydrolysis of C-steels were found. In any case organics evolution should be taken into account in further studies.

4.5. Iron-bentonite interactions

Metal corrosion was represented by an increase of the Fe-content in bentonite samples and the presence of corrosion products, mainly at heater contact. Probably most of the heater corrosion occurred at oxic conditions due to the corrosion products detected: goethite and hematite. However, oxygen may rapidly be depleted at the surface of steel by reactions of Fe-bearing minerals in the bentonites: pyrite, siderite, Fe(II) in octahedral sites of montmorillonite particles, etc. However, this redox buffer capacity is limited due to the low amount of reduced components, which it will depend on the initial composition of each bentonite. The possible anoxic corrosion originated some amount of Fe(II), which was transported by diffusion though the bentonite from heater contact. An increase of Fe(II) is observed at the heater contact (Figure 11 and Figure 13), being the content much lower than Fe(III). This Fe(II) precipitated as siderite and pyrite, as shown by XRD in different samples (Figure 5), but not in all bentonites. Therefore, redox conditions must have been locally different. However, it seems that oxygen was not completely depleted in the test. Magnetite was not detected in contrast to former ABM experiments [70]. In addition, variations in sulfur contents are insignificant.

5. Conclusions

Geochemical modifications of different bentonites (Asha 505, FEBEX, Rokle, IBECO and MX-80) used as engineered barriers were studied in the ABM5 experiment. In this medium large-scale *in situ* test, bentonite compacted blocks were artificially saturated with saline Äspö groundwater and heated up to 250°C.

The main change observed in all bentonites is the modification of exchangeable cation composition, explained on the basis of equilibration with Äspo saline groundwater enriched with Ca and Na salts. Calcium bentonites (FEBEX, Rokle, IBECO) increased their sodium content, and sodium bentonites (Asha 505, MX-80) increased their calcium content. Exchangeable magnesium decreased in all the samples, except in MX-80 block 1 located at the bottom of the column. The variation of the type of exchangeable cations in all bentonites seems to indicate that concentration tends to equilibrium with groundwater and to be homogeneous in the whole bentonite column, prevailing bivalent cations at exchange sites.

Cation exchange variations and/or salinity of the pore waters may explain the decrease of the external surface area values observed in all samples. However swelling capacity is not affected due to total surface are data is not modified.

A decrease on CEC values is observed towards heating surface, which may be related to high-temperature conditions, water vapor formation or to a modification of the crystal structure of the smectite clay particles, decreasing the layer charge.

In spite of available and increased magnesium content in the pore water, no other additional magnesium-bearing mineral phases and/or trioctahedral smectites were detected, as found in ABM1 and ABM2 experiment. Furthermore, transformation of montmorillonite to illite is discarded, probably to low variations in the potassium content both in pore waters and exchange sites.

Fe increased as a function of the heater contact. Heater corrosion provoked the increase of iron in the bentonite, and goethite, hematite and siderite were found as corrosion products. No magnetite was detected. Although the ratio of ferrous to ferric iron increased in the close vicinity of the C-steel heater, major Fe content is as Fe(III). No indications of Fe-montmorillonite have been detected.

The pore water chemistry depends on the composition and advection-diffusion rate of the infiltrating saline groundwater, and it is basically controlled by ion exchange reactions and dissolution/precipitation of the more soluble trace minerals of the bentonite. An advective-diffusion infiltration process of the conservative ions (Cl^-, Br^-, F^-) is observed towards the heater, but after 4.4 years of experiment the pore water is not at equilibrium in all bentonite blocks. The initial bentonite pore water was modified in all bentonite blocks, changing from mainly initial Na-Cl or Na-SO_4 water type towards a Na-Ca-Cl pore water in all bentonite blocks analysed, except for MX-80 block 1, which changes from Na-SO_4 to Na-Cl water-type. Probably water-vapor fluxes increased the salinity of the pore waters at the top part of the package. In any case, anion inventory indicates that saturated bentonites (including cation occupancy and pore water composition) are not equilibrated with external infiltrating ground water.

Supplementary Materials: The following are available online at www.mdpi.com/xxx/s1, Table S1. Mineral phases observed in the bentonite samples by means of XRD, FTIR and SEM techniques; Table S2. Positions and assignments of vibrational bands of dioctahedral smectites, kaolinite and illite; Table S3. Chemical composition of the solid phase (total fraction) for different samples obtained after dismantling of ABM5 experiment: Asha Block 28, Febex Block 25 and Rokle Block 11; Table S4. Chemical composition of the solid phase (total fraction) for different samples obtained after dismantling of ABM5 experiment: Ibeco Block 11, MX-80 Block 1; Table S5. Fe(II), Fe(II) and total Fe contents obtained after dismantling of ABM5 experiment; Table S6. Parameters deduced from the BET and t-plot treatment on the adsorption of N2 at 77 K from samples obtained after dismantling of ABM5 experiment, Table S7. Total cation exchange capacity (CEC) and cation exchange population prior and after dismantling of the ABM5 experiment (in meq/100g); Table S8. Soluble salts from aqueous leaching tests a 1:4 solid to liquid ration, in mg/L; Table S9. Ion inventory obtained from aqueous leaching tests, in mol/100g; Table S10. Calculated parameters and saturation indexes of the pore waters; Table S11. Chemical composition of the pore waters obtained by squeezing at 25 MPa for water vapour saturated FEBEX, IBECO RW C16, and MX-80 bentonites at initial conditions; Figure S1. XRD patterns of total fraction samples from ABM5 experiment; Figure S2. XRD patterns of oriented aggregate samples from ABM5 experiment (normal and after ethylene glycol and heating at 550 °C treatments); Figure S3. Wide scan XPS spectrum recorded from sample Rokle 4H at heater contact, Figure S4. Fe 2p XPS spectra recorded from samples con-

taining different concentrations of Fe(III) and Fe(II) standard compounds; Figure S5. Room temperature Mössbauer spectra recorded in a narrow range of velocities for Rokle samples: reference, 4H: close to heater interface, 5M: middle, and 6G: close to granite interface, i.e., at 1.67 cm, 5.00 cm and 8.33 cm from heater contact, respectively, Figure S6. N2 adsorption/desorption isotherms from reference and retrieved ABM5 samples.

Author Contributions: Conceptualization, A.M. Fernández, F.J. Marco; D. Svensson, P. Sellin; methodology, A.M. Fernández, F.J. Marco, D. Svensson; validation, A.M. Fernández, F.J. Marco, D. Svensson; formal analysis, A.M. Fernández, J.F. Marco, D. Svensson, P. Nieto, F.J. León, L. Robledo, M.A. Clavero, A. Cardona, S. Fernández; investigation, A.M. Fernández; P. Nieto, F.J., León, resources, CIEMAT, CSIC; data curation, A.M. Fernández, F.J. Marco, D. Svensson, P. Nieto, F.J. León, L. Robledo, M.A. Clavero; writing—original draft preparation, A.M. Fernández; writing—review and editing, A.M. Fernández, F.J. Marco, D. Svensson, P. Sellin. All authors have read and agreed to the published version of the manuscript.

Funding: This work was funded by the EURAD-Concord European Commission Project and CIEMAT. Financial support for grant RTI2018-095303-B-C51 funded by MCIN/AEI/10.13039/501100011033 and "ERDF A way of making Europe" is gratefully acknowledged.

Data Availability Statement: Not applicable.

Acknowledgments: We acknowledge to UCM (Madrid, Spain) and the Chemical Department from CIEMAT for performing the XRF, XRD, SEM and chemical analyses.

Conflicts of Interest: The authors declare no conflict of interest.

References

1. Svensson, D.; Sandén, T.; Olsson, S.; Dueck, A.; Eriksson, S.; Jägerwall, S.; Hansen, S. Alternative buffer material Status of the ongoing laboratory investigation of reference materials and test package 1. SKB TR-11-06; Svensk Kärnbränslehantering AB: Stockholm, Sweden, 2011, 146 pp.
2. Sandén, T.; Nilsson, U.; Svensson, D. ABM45 experiment at Äspö Hard Rock Laboratory. Installation Report. SKB Report P-18-20, 2018, 49 pp.
3. Kaufhold, S.; Dohrmann, R.; Ufer, K.; Svensson, D.; Sellin, P. Mineralogical Analysis of Bentonite from the ABM5 Heater Experiment at Äspö Hard Rock Laboratory, Sweden. *Minerals* **2021**, *11*, 669.
4. Sudheer Kumar, R.; Podlech, C.; Grathoff, G.; Warr, L.N.; Svensson, D. Thermally Induced Bentonite Alterations in the SKB ABM5 Hot Bentonite Experiment. *Minerals* **2021**, *11*, 1017.
5. Gordon, A.; Pahverk, H.; Börjesson, E.; Johanss, A.J. Examination of copper corrosion specimens from ABM 45, package 5. Technical Report TR-18-17, 2018, 27 pp.
6. Karnland, O; Olsson, S.; Nilsson, U. Mineralogy and sealing properties of various bentonites and smectite-rich clay materials. SKB TR-06-30, 2006, Svensk Kärnbränslehantering AB.
7. Slaughter M.; Earley, J. W. Mineralogy and geological significance of the Mowry bentonites, Wyoming. 1965. New York: Geological Society of America. Geological Society of America Special Paper 83.
8. Christidis, G.; Scott, P. W.; Marcopoulos, T. Origin of the bentonite deposits of Eastern Milos, Aegean, Greece: Geological, Mineralogical and Geochemical Evidence. *Clays and Clay Minerals* **1995**, *43*, 63 – 77.
9. Konta, J. Textural variation and composition of bentonite derived from basaltic ash. *Clays and Clay Minerals* **1986**, *34*, 257–265.
10. Přikryl, R.; Woller, F. Going underground: A new market for Czech bentonite in nuclear waste disposal. *Industrial Minerals* **2002**, *415*, 72–77.
11. Huertas, F.; Farina, P.; Farias, J.; Garcia-Sineriz, J.L.; Villar, A.M.; Fernandez, A.M.; Martin, P.L.; Elorza, F.J.; Gens, A.; Sanchez, M.; Lloret, A.; Samper, J.; Martinez, M.A. FEBEX Project. Full-scale Engineered Barriers Experiment for a Deep Geological Repository for High Level Radioactive Waste in Crystalline Host Rock. Updated Final Report 1994-2004. Technical Publication ENRESA 5-0/2006. 2006, pp. 590 (Madrid).
12. Fernandez, A.M.; Baeyens, B.; Bradbury, M.; Rivas, P. Analysis of the pore water chemical composition of a Spanish compacted bentonite used in an engineered barrier. *Physics and Chemistry of the Earth* **2004**, *29*, 105–118.
13. Shah, N. R. Indian bentonite: focus on the Kutch region. *Industrial Minerals* **1997**, *359*, 43–47.
14. Jackson, M.L. Soil Chemical Analysis. Advanced course. Revised Second Edition. Parallel Press. University of Wisconsin-Madison Libraries. Madison, Wisconsin, 2005, 930 pp.
15. Moore, D.; Reynolds, R. X-Ray diffraction and the identification and analysis of Clay Minerals. Oxford University Press, N.Y., 1989332 pp.
16. Newman, A.C.D. Chemistry of Clays and Clay Minerals. Mineral Society. Monograph Nº 6. Longman Scientific & Technical, 1987, 480 pp.

17. Wagner, C.D.; Davis, L.E.; Zeller, M.V.; Taylor, J.A.; Raymond, R.M.; Gale, L.H. Empirical atomic sensitivity factors for quantitative analysis by electron spectroscopy for chemical analysis. *Surf. Interface Anal.* **1981**, 3, 211-225.
18. Tarafder, P.K., Thakur, R. An optimised 1,10-Phenathroline method for the determination of ferrous and ferric oxides in silicate rocks, soils and minerals. *Geostandards and Geoanalytical Research*. **2012**, 37, 155-168.
19. Amman, L.; Bergaya, F.; Lagaly, G. Determination of the cation exchange capacity of clays with copper complexes revisited. *Clay Minerals* 2005, 40, 441-453.
20. Sawhney, B. L. Potassium and caesium ion selectivity in relation to clay mineral microstructure. *Clays and Clay Minerals 1970*, 18, 47-52.
21. Gregg, S. J.; Sing, K.S.W. Adsorption, Surface area and Porosity. Academic Press. 1982, 303 pp.
22. Keeling, P.S.; Kirby, E.C.; Robertson, R. H. S. Moisture adsorption and specific surface area. *J. Brit. Ceram. Soc.* **1980**, 79, 36-40.
23. Fernández, A.Mª.; Bath, A.; Waber, H.N.; Oyama, T. Annex 2: water sampling by squeezing drillcores. In: Pearson, F.J., Arcos, D., Bath, A., Boisson, J.Y., Fernández, A.Mª., Gäbler, H.-E., Gaucher, E., Gautschi, A., Griffault, L., Hernán, P., Waber, H.N., (Eds.). Geochemistry of Water in the Opalinus Clay Formation at the Mont Terri Rock Laboratory. FOWG No. 5, 2003, 171–199.
24. Fernández A.M., Caracterización y modelización del agua intersticial en materiales arcillosos: Estudio de la bentonita de Cortijo de Archidona. Ph. D. Thesis. CIEMAT, Madrid, 2004, 505 pp.
25. Fernández, A. M.; Sánchez-Ledesma, D. M.; Tournassat, C.; Melón, A.; Gaucher, E. C.; Astudillo, J.; Vinsot, A. Applying the Squeezing Technique to Highly Consolidated Clayrocks for Pore Water Characterisation: Lessons Learned from Experiments at the Mont Terri Rock Laboratory. *Applied Geochemistry* **2014**, 49, 2-21.
26. Entwisle, D.C.; Reeder, S. New apparatus for pore fluid extraction from mudrocks for geochemical analysis. In: Geochemistry of Clay-Pore Fluid Interactions. The Mineralogical Society Series. Chapman and Hall, 1993, 365–388.
27. Peters, C. A.; Yang, Y. C.; Higgins, J. D.; Burger, P. A. A preliminary study of the chemistry of pore water extracted from tuff by one-dimensional compression. Water-Rock Interaction, Kharaka & Maest (eds.), 1992, 741-745.
28. War, L. IMA–CNMNC approved mineral symbols. *Mineralogical Magazine*, **2021**, *85*, 291–320.
29. Svensson, D. The bentonite barrier. Swelling properties, redox chemistry and mineral evolution. PhD Thesis 2015. Lund University.
30. Kaufhold S.; Dohrmann R.; Sandén T.; Sellin P.; Svensson D. Mineralogical investigations of the alternative buffer material test - I. Alteration of bentonites. *Clay Minerals* **2013**, *48*, 149-213.
31. Fernández, A.M.; Kaufhold, S.; Sánchez-Ledesma, D.M.; Rey, J.J.; Melón, A.; Robredo, L.M.; Fernández, S.; Labajo, M.A.; Clavero, M.A. Evolution of the THC conditions in the FEBEX *in situ* test after 18 years of experiment: Smectite crystallochemical modifications after interactions of the bentonite with a C-steel heater at 100 °C. *Applied Geochemistry* **2018**, 98, 152 - 171.
32. Alburquenque, D.; Márquez, P.; Troncoso, L.; Pereira, A.; Celis, F.; Sánchez-Arenillas, M.; Marco, J.F.; Gautier, J.L.; Escrig, J. $LiM_{0.5}Mn_{1.5}O_{4-\delta}$ (M = Co or Fe) spinels with a high oxidation state obtained by ultrasound-assisted thermal decomposition of nitrates. Characterization and physicochemical properties. *J. Solid State. Chem.* **2020,** 284, 121175.
33. López, G.P.; Castuer, D.G.; Ratner, B. XPS 0 1s Binding Energies for Polymers Containing Hydroxyl, Ether, Ketone and Ester Groups. *Surf. Interf. Anal.* **1991**, 17, 267-272.
34. Marco, J.F.; Gancedo, J.R.; Ortiz, J.; Gautier, J.L. Appl. Characterization of the spinel-related oxides $Ni_xCo_{3-x}O_4$ (x=0.3,1.3,1.8) prepared by spray pyrolysis at 350°C. *Surf. Sci.* **2004**, 227, 175-186.
35. Smirnov, M. Y.; Kalinkin, A.V.; Bukhtiyarov, V.L. X-ray photoelectron spectroscopic study of the interaction of supported metal catalysts with NOx. *J. Struct. Chem.* **2007**, 48, 1053-1066.
36. Meskinis, S.; Vasiliauskas, A.; Androlevicious, M.; Peckus, D.; Tamulevicius, S.; Viskontas, K. Diamond Like Carbon Films Containing Si. *Structure and Nonlinear Optical Properties Materials* **2020**, 13, 1003.
37. Bancroft, G.M. Mössbauer Spectroscopy: An Introduction for Inorganic Chemists and Geochemists. McGraw Hill, 1973, Maidenhead, Berkshire, England.
38. Maddock, A.G. Mössbauer Spectrometry in Mineral Chemistry. In: Chemical Bonding and Spectroscopy in Mineral Chemistry (F.J. Berry and D.J. Vaughan, editors). 1985, 141-208. Springer Netherlands.
39. Coey J. M. D. Clay minerals and their transformations studied with nuclear techniques: The contribution of Mössbauer spectroscopy. *Atomic Energy Review* **1980**, 18, 73-124.
40. Heller-Kallai, L.; Rozenson I. The use of Mössbauer spectroscopy of iron in clay mineralogy. *Physics and Chemistry of Minerals* **1981**, 7, 223-238.
41. De Grave, E.; Vandenbruwaene, J.; Elewaut, E. An^{57}Fe Mössbauer effect study on glauconites from different locations in Belgium and northern France. *Clay Minerals* **1985**, 20, 171-179.
42. Dainyak, L. G.; Drits, V. A. Interpretation of Mössbauer spectra of nontronite, celadonite and glauconite. *Clays and Clay Minerals*, **1987**, 35, 363-373.
43. Dainyak, L. G.; Drits, V. A.; Heifits, L.M. Computer simulation of cation distribution in dioctahedral 2:1 layer silicates using IR-data: Application to Mössbauer spectroscopy of a glauconite sample. *Clays and Clay Minerals* **1992**, 40, 470-479.
44. Pelayo, M.; Marco, J.F.; Fernández, A.M.; Vergara, L.; Melón, A.M.; del Villar, L.P. Infrared and Mössbauer spectroscopy of Fe-rich smectites from Morrón de Mateo bentonite deposit (Spain). *Clay Minerals 2018*, 53, 17-28.
45. Murad, E.; Johnston, J. H. Iron Oxides and Oxyhydroxides. Mössbauer Spectroscopy Applied to Inorganic Chemistry. 1987, Volume 2, Chapter 12, pp. 507-582. Gary J. Long, ed. Plenum, New York.
46. Vandenberghe, R. E.; De Grave, E. Application of Mössbauer spectroscopy in earth sciences. "Mössbauer Spectroscopy. Tutorial Book". 2013, Chapter 3, pp. 91-186 .Y. Yoshida and G. Langouche, eds. Springer-Verlag Berlin Heidelberg.

47. Dang, M.Z.; Rancourt, D.G.; Dutrizac, J.E.; Lamarche, G.; Provencher, R. Interplay of surface conditions, particle size, stoichiometry, cell parameters, and magnetism in synthetic hematite-like materials. *Hyperfine Interactions* **1998**, 117, 271–319.
48. Goss, C. J. The kinetics and reaction mechanism of the goethite to hematite transformation. *Mineralogical Magazine* **1987**, 51, 437-451.
49. Hernández, T.; Sánchez, F.J.; Moroño, A.; Aristu, M.; Marco J.F. Effect of irradiation on the stability of the corrosion layer produced in EUROFER by contact with lithium ceramics. *Journal of Nuclear Materials* **2021**, 545, 152614.
50. Sing, K.S.W.; Everett, D.H.; Haul, R.A.W.; Moscou, L.; Pierotti, R.A.; Rouquerol, J.; Siemieniewska, T. Reporting physisorption data for gas/solid systems with Special Reference to the Determination of Surface Area and Porosity. *Pure Appl. Chem.* **1985**, 57, 603-619.
51. Fernández, A.M.; Sánchez-Ledesma, D.M.; Melón, A.; Robredo, L.M.; Rey, J.J.; Labajo, M.; Clavero, M.A.; Fernández, S.; González, A.E. Thermo-hydro-chemical (THC) behaviour of a Spanish Bentonite after dismantling Heater#1 and Heater#2 of the FEBEX *in situ* test at the Grimsel Test Site. Nagra Working Reports. NAB 16-25, 2018, 583 pp.
52. Fernández, A. M.; Rivas, P. Pore water chemistry of saturated Febex bentonite compacted at different densities. In: Alonso, E.E., Ledesma, A. (Eds.), Advances in understanding Engineered Clay Barriers. A.A. Balkema Publishers, Leiden, 2005, 505-514.
53. Parkhurst, D.L.; Appelo, C.A.J. Description of input and examples for PHREEQC version 3—A computer program for speciation, batch-reaction, one-dimensional transport, and inverse geochemical calculations: U.S. Geological Survey Techniques and Methods, book 6, chap. A43, 2003, 497 pp.
54. Blanc, P. Thermoddem: update for the 2017 version. Report BRGM/RP-66811-FR, 2017, 20 pp.
55. Svensson, P.D., Hansen, S. Redox chemistry in two iron-bentonite field experiments at Äspö Hard Rock Laboratory: and XRD and Fe K-edge XANES study. *Clays and Clays Minerals* 2013, 61, 566-579.
56. Olsson, S.; Jensen, V.; Johanesson, L. E.; Hansen; E., Karnland, O.; Kumpulainen, S.; Kirivanta, L.; Svensson, D.; Hansen, S.; Lindén, J. Prototype Repository - Hydromechanical, chemical and mineralogical characterization of the buffer and backfill material from the outer section of the Prototype Repository. Swedish Nuclear Fuel and Waste Management Co (SKB) 2013. Technical Report TR-13-21.
57. Missana, T., Alonso, U., Fernández, A.M., García-Gutiérrez, M., 2018. Analysis of the stability behaviour of colloids obtained from different smectite clays. *Applied Geochemistry* 2018, 92, 180-187.
58. Dohrmann R.; Olsson S.; Kaufhold S.; Sellin P. Mineralogical investigations of the alternative buffer material field test - II. Exchangeable cation population rearrangement. Clay Minerals 2013, 48, 215-233.
59. Kaufhold, S.; Dohrmann, R.; Ufer, K.; Kober, F. Interactions of bentonite with metal and concrete from the FEBEX experiment - mineralogical and geochemical investigations of selected sampling sites. *Clay Miner.* 2018, 53, 745–763.
60. Dohrmann, R.; Kaufhold, S. Characterisation of the second package of the alternative buffer material (ABM) experiment – II Exchangeable cation population rearrangement. *Clays Clay Miner.* 2017, 65, 104–121.
61. Dohrmann, R.; Kaufhold, S. Cation exchange and mineral reactions observed in MX 80 buffer samples from the Prototype repository *in situ* experiment in Äspö, Sweden. *Clays and Clay Minerals* 2014, 5, 357-373.
62. Heuser, M.; Weber, C.; Stanjek, H.; Chen, H.; Jordan, G.; Schmahl, W.W.; Natzeck, C. The interaction between bentonite and water vapor. I: Examination of physical and chemical properties. Clays Clay Miner. 2014, 62, 188–202.
63. Kaufhold, S.; Dohrmann, R. Stability of bentonites in salt solutions: II. Potassium chloride solution. Initial step of illitization?. *Applied Clay Science* **2010**, 49, 98-107.
64. Karnland, O.; Olsson, S.; Nilsson, U. Mineralogy and sealing properties of various bentonites and smectite rich clay materials. SKB Technical Report TR-06-30, 2006, SKB, Stockhlom, Sweden, 112 pp.
65. Herbert, H.-J.; Kasbohm, J.; Sprenger, H.; Fernández, A.M.; Reichelt, C. Swelling pressures of MX-80 bentonite in solutions of different ionic strength. *Physics and Chemistry of the Earth* **2008**, 33, 327-342.
66. Kaufhold, S.; Dohrmann, R. Effect of extensive drying on the cation exchange capacity of bentonites. *Clay Minerals* **2010**, 45, 441-448.
67. Fernández, A.Mª; Cuevas, J.; Rivas, P. Pore water chemistry of the FEBEX bentonite. In: Hart, K.P. and Lumpkin, G.R. (Eds.), Scientific Basis for Nuclear Waste Management XXIV. *Mat. Res. Soc. Symp. Proc.* **2001**, 663, 573-588.
68. Wersin, P. Geochemical modelling of bentonite pore water in high-level waste repositorys. *Journal of Contaminant Hydrology* **2003**, 61, 405-422.
69. Bradbury, M.H.; Berner, U.; Curti E.; Hummel W.; Kosakowski, G.; Thoenen, T. The Long Term Geochemical Evolution of the Nearfield of the HLW Repository. 2014. Nagra Technical Report NTB 12-01.
70. Wersin, P.; Hadi, J.; Jenni, A.; Svensson, D.; Grenèche, J.-M.; Sellin, P.; Leupin, O.X. Interaction of Corroding Iron with Eight Bentonites in the Alternative Buffer Materials Field Experiment (ABM2). *Minerals* **2021**, *11*, 907.